AD/A-001 040

TURBULENT WAKE BEHIND SLENDER BODIES INCLUDING SELF-PROPELLED CONFIGURATIONS

R. C. Swanson, Jr., et al

Virginia Polytechnic Institute and State University

Prepared for:

Office of Naval Research

September 1974

AD/A001 040

REPORT DOCUMENTATION PAGE		READ INSTRUCTIONS BEFORE COMPLETING FORM
1. REPORT NUMBER	2. GOVT ACCESSION NO.	3. RECIPIENT'S CATALOG NUMBER
4. TITLE (and Subtitle) TURBULENT WAKE BEHIND SLENDER BODIES, INCLUDING SELF-PROPELLED CONFIGURATIONS		5. TYPE OF REPORT & PERIOD COVERED Final Report
		6. PERFORMING ORG. REPORT NUMBER VPI Aero-024
7. AUTHOR(s) R. C. Swanson, Jr., J. A. Schetz and A. K. Jakubowski		8. CONTRACT OR GRANT NUMBER(s) N00014-72-A-0136-0004
9. PERFORMING ORGANIZATION NAME AND ADDRESS Aerospace and Ocean Engr. Dept. Virginia Polytechnic Institute and State Univ. Blacksburg, Virginia 24061		10. PROGRAM ELEMENT, PROJECT, TASK AREA & WORK UNIT NUMBERS NR-062-481
11. CONTROLLING OFFICE NAME AND ADDRESS Office of Naval Research Arlington, Virginia 22217		12. REPORT DATE September, 1974
		13. NUMBER OF PAGES 88
14. MONITORING AGENCY NAME & ADDRESS(If different from Controlling Office)		15. SECURITY CLASS. (of this report) Unclassified
		15a. DECLASSIFICATION/DOWNGRADING SCHEDULE

16. DISTRIBUTION STATEMENT (of this Report)

Approved for public release; distribution unlimited

17. DISTRIBUTION STATEMENT (of the abstract entered in Block 20, if different from Report)

18. SUPPLEMENTARY NOTES

19. KEY WORDS (Continue on reverse side if necessary and identify by block number)

Turbulent Wakes
Self-propelled Body
Turbulent Shear Flow Calculations

20. ABSTRACT (Continue on reverse side if necessary and identify by block number)

The turbulent wakes behind a streamlined drag body, a jet-propelled body, and a propeller-driven body are studied experimentally in a subsonic wind tunnel at a principal nominal free-stream velocity of 206 ft/sec. The wakes produced by the latter two bodies are momentumless. Mean flow data taken at five axial stations (X/D = 2, 5, 10, 20, and 40) downstream of the sterns of

these bodies include velocity and static pressure distributions. The stream-wise variation of the maximum values of axial turbulence intensity and radial shear stress are also presented.

The mean flow data for the wake behind the drag body compare favorably with previous experiments and establish a rigid reference for the wakes behind slender, self-propelled configurations. The downstream rate of decay of $\left|(U_E - U_c)_{max}/U_E\right|$ is essentially the same for the drag and propeller-driven bodies, whereas the decay for the jet-propelled body is substantially faster. A self-similar character is exhibited in the wake of the drag body, but the wake of the propeller-driven body appears to be self-similar in the usual sense only in the inner region. As for the basic turbulence behavior, the magnitude of the axial turbulence intensity is greater for the jet-propelled model than the other models, and the absolute value of the radial shear stress is greater (beyond $X/D = 2$) for the propeller driven model. The rate of decay of $(\sqrt{u'^2})_{max}$ is faster for the propeller-driven model than the jet-propelled model; however, the rate of decrease of radial shear stress is faster for the jet-propelled model.

A comparison of the axial variation of $\left|(U_E - U_c)_{max}/U_E\right|$ with numerical predictions using a turbulent kinetic energy method shows very good agreement for the drag and jet-propelled bodies. The shear stress trends are predicted well in all cases.

ia

September 1974   VPI-Aero-024

TURBULENT WAKE BEHIND SLENDER BODIES

INCLUDING SELF-PROPELLED CONFIGURATIONS

by

R. C. Swanson, Jr., J. A. Schetz and
A. K. Jakubowski

Aerospace and Ocean Engineering Department

ii

TABLE OF CONTENTS

LIST OF FIGURES

NOMENCLATURE

a_1	ratio of turbulent shear stress to turbulent kinetic energy
C_D	drag coefficient
C_T	thrust coefficient
D	maximum diameter of models
D_1	diameter of propeller
D'	drag
E	D.C. voltage
e	RMS voltage
J	advance diameter ratio
k	turbulent kinetic energy
m	torque
n	revolutions per second
P	pressure
P_I	injection pressure
Q	dynamic pressure
R_e	Reynolds number
R_o	maximum radius of models
T	thrust
U, V_R, V_T	mean velocity components in the X, R, ϑ directions
u', v'	turbulent velocity components in the X, R directions
$\sqrt{\overline{u'^2}}$	axial turbulence intensity
$\overline{u'v'}$	radial Reynolds shear stress
V	mean total velocity
X, R, θ	axial, radial, and tangential coordinates

ε	eddy viscosity
η_p	propeller efficiency
ρ	density
σ_R	propeller solidity
τ	turbulent shear stress
ψ	yaw angle

Subscripts

B	barometric
C	center of wake
E	edge of wake
M	mean value
m	measured value
s	static
t	total

1. INTRODUCTION

Recently there has been considerable interest expressed in turbulent wake flows with zero net-momentum defect. Such flows occur behind a wide variety of self-propelled bodies, including airplanes and hydrodynamic vehicles. Among the many practical problems encouraging investigation of these configurations are submarine detection and dispersion of pollution from aircraft propulsion units. A complete understanding of ordinary wake flows is necessary in order to treat these more complicated wake flows. At this point there is little information concerning the turbulent fluid motion behind not only self-propelled bodies but also slender, axisymmetric bodies.

Due to the highly complex nature of turbulent flows, especially those with non-homogeneous and non-isotropic fluctuating motion, analytical investigations are seriously impeded without the application of heuristic models for the turbulence contributions to the mathematical flow descriptions. This is particularly true for higher order turbulence models. Therefore, there is an imperative need for turbulent experimental data and the accompanying empirical formulations. Table 1 provides a representative yet not exhaustive summary of the available experimental data for subsonic, axisymmetric turbulent wakes. This clearly demonstrates that the majority of the research thus far is related to unstreamlined, axisymmetric bodies. Moreover, only two distinctly different self-propelled cases have been examined previously. Several experiments were conducted in which the zero-momentum wake was

1

TABLE 1

Summary of Subsonic, Axisymmetric Turbulent Wake Experiments

Author	Year	Ref. No.	Momentumless	Mean Flow	Turbulent Properties	Configuration
Hall and Hislop	1938	17		x		1 x 2 Cylinder
Cooper and Lutzky	1955	16		x	x	Thin Disks
Ilizarova and Pochkina	1962	18		x		6.67 x 1 Body of Revolution
Ridjanovic	1963	5	x	x	x	Circular Disk
Carmody	1964	7		x	x	Circular Disk
Wang	1965	6	x	x	x	Circular Disk
Naudascher	1965	8	x	x	x	Circular Disk
Ginevskii, Pochkina, and Ukhanova	1966	25	x	x	x	Circular Disk
Buchinskaya and Pochkina	1966	26		x		6 x 1 Ellipsoid
Chevray	1968	10		x	x	6 x 1 Spheroid
Bukreev, Kostomakha, and Lytkin	1972	13		x	x	Slender Body (8:1 Prolongation)

TABLE 1 (Cont.)

Summary of Subsonic, Axisymmetric Turbulent Wake Experiments

Author	Year	Ref. No.	Momentumless	Mean Flow	Turbulent Properties	Configuration
Hokenson and Schetz	1973	11		x	x	Sphere
Bukreev, Kostomakha, and Lytkin	1974	14		x	x	Sphere and Slender Body
Gran	1974	9	x	x	x	Rankine Ovoid
Swanson and Chieng	1974	Present	x	x	x	Slender Bodies

established with a circular disk and a central jet providing sufficient thrust to balance the drag of the disk (i.e. Refs. 5 and 8 are typical). Gran (Ref. 9), on the other hand, investigated the momentumless wake of a propeller-driven, aerodynamic shaped Rankine ovoid ($U_\infty = 64$ ft/sec). Thus preceding experiments have either been for bodies (circular disk) of little practical interest or for very low Reynolds numbers ($Re_D \simeq 6 \times 10^4$). Also, it is indeed very difficult to compare such studies performed with two entirely dissimilar bodies and at different test conditions. For these reasons a more definitive and systematic experimental investigation is in order.

The steady state equivalent of an axisymmetric body immersed in an incompressible fluid and moving at a constant speed may be simulated in the wind tunnel through the principle of relative motion. Even though a simulation could be achieved in a towing tank, the wind tunnel is a better testing facility in this instance because of the sample time available for turbulence measurements. In this particular experimental undertaking the importance of Reynolds number (Reynolds similarity) was recognized and a concerted effort was made to maximize it. This program was conceived to provide a systematic comparison of the turbulent wakes behind slender bodies with identical forebody shape by varying through the following cases: 1) Pure drag body, 2) self-propelled by axial fluid injection, 3) self-propelled with a well designed propeller. Here "well designed" is taken to mean matched to the nominal operating conditions of the experiment; however, this is not to be construed as "optimum designed". Tests were done in a large

(6 ft. x 6 ft.), low speed wind tunnel at a high speed (206 ft/sec), so
that a Reynolds number based on diameter of nominally 6.18×10^5 could
be achieved. This is more than an order of magnitude larger than pre-
vious propeller-driven laboratory tests. For each model, mean flow
stagnation and static pressure measurements (axial velocity) were made
with a pitot-static tube in the radial direction at five axial stations
(X/D = 2, 5, 10, 20, and 40). Flow angularity was determined with a
wedge type directional probe, and a Kiel probe was employed to measure
total pressure when required. Since the inclination in the vertical
X-R plane of the flow behind the propeller-driven model was less than
1° with repect to the free stream direction (positive X-axis), the
induced swirl velocity (tangential velocity) was estimated from yaw
angle measurements. The following turbulence intensity and Reynolds
shear stress values were obtained using straight and slanted hot wires,
respectively: $\sqrt{\overline{u'^2}}$, $\sqrt{\overline{v'^2}}$, $\sqrt{\overline{w'^2}}$, $\overline{u'v'}$, $\overline{u'w'}$. In this report only
the mean flow field and its properties are evaluated in detail and com-
pared with existing data. Obviously, it is quite impossible to
divorce the discussion from all turbulence considerations; therefore,
the information that exemplifies the interrelationship between the mean
and fluctuating fluid motion is included in the development of the
results section. The remaining turbulence data and an analysis of same
is provided in Ref. 24. Finally, numerical predictions of the down-
stream decay of the wake profiles, as dictated by the mean axial velo-
city deficit and radial Reynolds shearing stress, using initial station
data are presented. These calculations are made by making boundary

layer type assumptions and solving the corresponding governing flow equations (parabolic partial differential equations) with a finite difference technique (Ref. 19). It must be emphasized that the primary effort here was experimental, and the computations serve as a delineation of present analytical capability to evaluate conventional and momentumless wakes.

In the first section of this report, a complete description of the equipment and test methods employed in the research is given. The techniques applied in data reduction are also included. Then the experimental results are presented and discussed. The numerical predictions are given last.

2. FACILITIES AND MODELS

2.1 Wind Tunnel

Tests were conducted in the VPI & SU Low-Speed Wind Tunnel. The main test section is 6 ft. x 6 ft. long. A general description of the tunnel along with a drawing of the complete planview is given in Fig. 1 in Appendix "C". The tests described here were all conducted at 9.5 inches of H_2O which corresponds to a nominal speed of 206 ft/sec. By constant monitoring, the tunnel Q value was maintained to within ±2% of the desired value. The turbulence factor (ratio of effective Re to test Re) of the air stream was 1.08. Before initiating any testing the tunnel was run for 15-30 minutes so as to insure that uniform conditions had been achieved, in particular, temperature equilibrium of the air stream. This was especially significant with regards to hot wire testing where temperature variation is exceedingly important, i.e. minimization of drift in electronics equipment.

2.2 Wind Tunnel Models

There were three models. All models had a maximum diameter of 6.0 inches and were either 68 or 72 inches long. They were supported on the centerline of the tunnel by a thin strut (maximum thickness of .5 inches and either a 9.5 or 10.375 inch chord) that extended from the top of the tunnel. Each had a parabolic nose, a 3 ft. cylindrical section middle body, and a pointed stern. When a model was located in the wind tunnel, it was initially centered with respect to the walls, and the stern extended just beyond the first cross section of the

7

interchangeable test section (Fig. 1).

2.2.1   Drag Body Model

A drawing of the drag body, which was called model #1, is shown in Fig. 2. The nose and stern parts of the model were constructed from wood, and the center section was made from aluminum.

2.2.2   Jet-Propelled Model

The model which employed air injection propulsion, referred to as model #2, had a plexi-glass nose, an aluminum middle section, and a stern formed by a slender, plexi-glass, tear drop shaped center body held in position by four copper flow vanes spaced 90 degrees apart. Air was injected through a 1 inch peripheral slot at the end of the parallel middle body. A photograph of the model is shown in Fig. 3, and a scaled drawing is given in Fig. 4. The air for injection was supplied by 150 psi compressors and stored in a 56.52 cu. ft. tank. The feed line from the tank to the model was a 3 inch pipe. Air taken from the tank was brought through a control valve and a strut into a plenum chamber in the model. The strut was comprised of 17 parallel .25 inch diameter copper tubes and two .5 inch diameter pipes, one at the leading edge and the other at the trailing edge. It was given a smooth surface and airfoil shape by covering it with polyester body filler. Two 1 ft. long and 4 inch wide pieces of iron bent at right angles, one on each side of the strut, were used to attach the strut to the top of the tunnel. All holes in the angle irons were slotted

in order to provide vertical and lateral adjustment capability for aligning the model. The plenum chamber was vented with a series of .3125 inch diameter peripheral holes spaced 1 inch apart, and the air leaving these holes went through a series of course and fine screens. These screens served the dual purpose of flow straightners and turbulence reducers.

For this model, tests were conducted to determine the necessary pressure, measured at the entrance point of air into strut system, to produce the thrust to balance the drag exerted by the body on the fluid. This pressure was found to be 112 psia and was designated as P_I. Due to fluctuations in this pressure, $\pm$ .2 psia, it was constantly monitored on a Heise pressure gauge (Model # C-5332). This gauge is sensitive to pressure changes as small as .05 psia.

2.2.3 Propeller-Driven Model

The propeller-driven model, shown in Fig. 5 and designated model #3, was the drag body model fitted internally with a Model 2M145 Dayton .5 HP, 10,000 rpm AC/DC motor operated DC (overloaded to 12,200 rpm). Any variations in rpm during testing were detected by electronic sensor and oscilloscope read out. A 23.375 inch long, .25 inch diameter stainless steel shaft was turned by the motor. Even though this motor was self-cooled with a fan, water cooling was provided due to the overload operating conditions. Both the motor casing and collar were wrapped with .1875 inch diameter copper tubing so as to provide motor and bearing cooling. There was constant monitoring of motor temperature in order to prevent irreparable damage

to the motor from overheating; replacement of the brushes was re-
quired. A maximum temperature of 127°F was reached. The propeller was
a 6.0 inch diameter, three bladed, plastic, model airplane propeller.
The blades were heated at the root and twisted with a special jig to
yield a higher pitch (originally 3 inches) in order to operate
efficiently at the high air speed of the tests. Propellers with a
variety of pitches were tested in order to find the appropriate pro-
peller, i.e. produce sufficient thrust to match drag of model #3. Com-
plete details concerning the testing of the propellers and the results
obtained are given in Appendix "A". In each case performance was
analyzed by the change of both thrust coefficient C_T and efficiency η_p
with advance ratio J (all performance terms are defined in Appendix
"A"). After considerable testing a propeller with a forward speed to
rotational speed ratio of 2.46, defined as the experimental mean dia-
meter pitch, and an apparent efficiency of .680 was selected. It must
be emphasized that the size of the propeller was scaled with respect
to the size of the wake and not the size of the body.

2.3 Instrumentation

2.3.1 Pressure Measurements

The mean flow data were obtained with the following probes: 1)
Pitot-static tube, 2) Yaw head tube, 3) Kiel tube. Dynamic and
static pressure measurements were made with a .0625 inch diameter
straight pitot static probe with static ports located .375 inches
from the tip; it was constructed by United Sensor and is shown in
Fig. 7. The United Sensor Model No. W-187 yaw head probe, a wedge-type

flow direction sensor with static and total pressure ports .1875 inches
from the tip of the wedge (Fig. 8), was used to find the flow yaw
angle variation for the propeller-driven model. Finally, to insure
the best possible accuracy for the measurement of total head when the
flow in the wake was skewed with respect to the free stream direction,
a Kiel probe (United Sensor Type KC) with a .25 inch diameter Venturi
sensing head and a .125 inch diameter probe was used. This probe is
insensitive to pitch and yaw angles up to angles of 40° or more
measured from the axis of the head. The pressures were measured on
either a Datametrics Type 523-13 differential pressure transducer
(range of 0-10 inches of H_2O) and/or an adjustable-angle multiple
manometer (a conventional manometer bank with tubes in front of a
lined glass plate), depending upon the number of readings required
simultaneously. All pressure transducer signals were displayed on
either a DS-100 Doric Integrating Microvoltmeter and/or Hewlett
Packard strip chart recorders. The DC digital voltmeter was equipped
with a variable sample rate and a four-figure read out. The recorders
are high speed, two channel potentiometric recorders with a maximum
deflection of 10 inches, accuracy of 0.1% of full scale setting, and
response time of 0.25 seconds. A Digitec Electronic Manometer (Model
277-3) with digital read out was used to monitor the tunnel Q.

2.3.2 Hot Wire Measurements

The turbulence data were obtained with straight wire (TSI Model
#1210) and 45° slant wire (TSI Model #1213) hot wire probes. Both
platinum plated tungsten wires were .00015 inches in diameter and had

an equilibrium response time of approximately .01 seconds. Also, the

cold resistance of the wires was 5-7 ohms, and they were operated at

a resistance 50% greater than the cold value (i.e. overheat ratio of

1.5). The signals were processed through a Thermo Systems Module

#1050 constant temperature anemometer and a Thermo Systems Module

#1051-6 (Power Supply) and read on a DISA 55D35 RMS digital voltmeter.

This anemometer has a high frequency filter (removes signals above 100

kilohertz or 400 kilohertz), but it has no low frequency filters.

Linearization of output of anemometer was not necessary because of low

amplitude signals for the flow field investigated. The RMS voltmeter

has a signal response range of 1 hertz to 400 kilokertz, integrator

time constants from .1 to 30 seconds, and an accuracy of .5% of the

full scale deflection. The straight wire probe was rotated 90° at each

position (as a check on the symmetry of the turbulent flow field) and

the slant wire probe was rotated 180° in each of two mutually orthogonal

planes in order to obtain the 3-component turbulent intensities and

Reynolds' stresses. This was accomplished automatically with a spe-

cially constructed apparatus to be described shortly.

2.3.3 Traversing Probe Mount

All probes were traversed through the wake at various axial

stations by an automatic traversing mount that is visible in Fig. 6.

This traverse was approximately 50.5 inches high and had a vertical

translation movement of 4 ft. The horizontal range was 5.5 inches

to either side of the center point. Vertical and horizontal motion was

controlled with variable speed motors; that is, regular DC motors in

series with potentiometers. The probe support was attached to the traverse in the manner shown in Fig. 3. It was 23.25 inches long and held both the pitot-static tube, interchangeable with other mean flow probes, and hot-wire support in position. The pitot tube was situated 2.9375 inches above the hot-wire support. The location of these probes was recorded on a Model 2D-3 (F. L. Moseley Co.) X-Y plotter. This means that the exact position of the probes was determined to within ±.016 inches. In order to rotate the hot-wire probes the hot-wire probe support was inserted into one end of a slotted aluminum cylinder and held in position with set screws. An aluminum blade was attached to the other end so as to make contact with miro-switches that were placed either 90 or 180 degrees apart on a slotted .0625 inch thick circular aluminum plate. A small DC motor was used to rotate the hot-wire probe support. Rotation was controlled with a remote switch that indicated orientation of probes. This switch was on the same control panel as the horizontal traverse speed control. Both this unit and the vertical speed control, which was a different unit, included variable speed capability.

3. EXPERIMENTAL PROCEDURE

3.1 Calibration Procedure

Before a model and the traverse were installed the hot-wire probes and the yaw head probe were calibrated. A variable height cast iron support stand with a rotating tripod mechanism was used to make these calibrations. A protractor with pointer was fixed to the tripod part in order to define the inclination of the probe. To obtain the dynamic pressure and probe measurement at the same point in the flow simultaneously a correlation between the tunnel Q value and the local Q value was formed. All probe supports were extended sufficently far beyond the placement of the stand to minimize stand interference effects.

Both straight and slant hot wire DC voltage measurements were taken for local Q valu.s between 5 and 10 inches of H_2O in increments of 1 inch of H_2O. Then the slant wire DC voltage readings for vertical plane angles between -6 and +6 degrees in increments of 2° were obtained. The angle settings were accomplished manually. Since the tunnel was stopped each time to do this, data was taken only when the tunnel temperature was approximately the same. These calibrations were done numerous times in order to have calibration curves, E versus V and E versus θ, for a complete range of temperatures.

The directional sensitivity probe was calibrated by first orienting the probe in the horizontal plane so that static port 2 was on the lower surface of the wedge (Fig. 8). The static pressure

14

difference $\Delta P = P_2 - P_3$ and the individual pressures P_2, P_3, and P_t were measured in 2° steps from -10° to +10°. Then the probe was rotated 180° and the same values recorded again. In each of the above cases data was taken for tunnel Q's of 7, 9, and 10 inches of H_2O. By plotting $(P_2-P_3)/(P_t-P_s)$ versus ψ for both orientations the free stream flow angularity was determined, i.e. ψ corresponding to point of intersection. Deviations in the calibration due to velocity sensitivity were not significant.

3.2 Procedure to Establish Momentumless Condition

The zero net momentum condition was required for the injection and propeller-driven models. Initially the traverse was placed at station $X/D = 5$, so as to exclude the effects associated with the tail and to include a definitive excess region in the velocity profile, and the pitot static probe was aligned along the axis of the body. In the case of model #2 dynamic pressure scans were taken for a range of P_I values (i.e. different ratios of jet velocity to free stream velocity) that were suggested by preliminary testing. Application of a cylindrical control volume analysis, where the momentum flux past any transverse section of the wake (constant for all stations) is equated to that of the oncoming free stream, yields the following expression for drag of an axisymmetric body:

$$D' = \rho \int_o^R U(U_E - U)2\pi R \; dR + \int_o^R (P_2-P_1)2\pi R \; dR$$

$$= 4\pi \int_o^R [\sqrt{QQ_E} - Q] \; R \; dR + \int_o^R (P_2-P_E)2\pi R \; dR + \int_o^R (P_F-P_1)2\pi R \; dR$$

(1)

where the subscript E means edge of shear layer, and R is sufficiently large so as to include the entire diffusion zone at a given X/D. The Q and local static pressure variations were integrated to determine the value of P_I necessary to satisfy $D \approx 0$. This calculation neglects the contributions from the viscous stresses (higher order terms) and turbulence (negligibly small in comparison to mean flow) that normally appear in the longitudinal Reynolds equation. For each injection pressure the drag values for horizontal and vertical scans were averaged.

In the case of model #3 pressure traverses were taken for a range of rpm values of the propeller. Again equation (1) was used in an interative experimental procedure to find the momentumless operating condition.

3.3 Location of Center of Wake

The following steps were required to establish the center of the wake at different axial stations for all models tested:

(1) The pitot-static tube was located in line with the tail of the model being tested.

(2) After the tunnel was started and the flow given time to stabilize (usually 15-30 minutes), a slow dynamic pressure scan of the wake of the model was made in both the horizontal and vertical directions. This was done to check for asymmetry resulting from improper alignment of model with the free stream flow direction (positive X-axis).

(3) If asymmetry was evident in step (2), the tunnel was stopped, and adjustments were made in the position of the model

support as prescribed by preliminary scans. These corrections and repetition of step (2) were continued until proper alignment had been achieved.

(4) The vertical center, indicated by dynamic pressure variation on strip chart recorder, was located while holding the horizontal position fixed.

(5) The horizontal center was established while maintaining vertical center established in step (4). Note, steps (4) and (5) could have been reversed.

(6) Steps (4) and (5) were repeated several times so as to determine center as accurately as possible.

3.4 Data Acquisition Procedure

3.4.1 Mean Flow

Once the center was established for a model, measurements were taken in the following order, where starred steps pertain only to the propeller-driven model:

(1) With the traverse at station $X/D = 5$ the yaw head probe was installed. The free stream yaw angle was found so that the pitot-static tube could be aligned with the free stream flow.

(2) The pitot-static tube was placed on the probe support, and the tunnel was again started. Horizontal and vertical pressure traces were made.

(3) Center position of the wake was checked, and corrections were made if necessary. The pressure scans were integrated

again to insure the zero net-momentum condition, and correc-
tions to either P_I or the rpm, in the cases of models #2 and
#3, were made if necessary.

(4) Dynamic and static pressure scans were made in the vertical
direction. Starting at 1 inch above the center of the wake,
measurements were taken at discrete .25 inch intervals.
Static pressures were recorded at .5 inch increments for
models #1 and #2.

(5)* The pitot-static tube was replaced with the directional probe.
Data was taken at .25 inch intervals.

(6)* To minimize the effects of flow angularity on the pressure
measurements of model #3 total pressure values were taken at
each point with a Kiel probe.

3.4.2 Hot Wire Measurements

(7) A straight wire was inserted in the hot-wire probe support
and adjusted to lie in the vertical radial plane. DC and
RMS (root-mean-square) signals were recorded at each .25 inch
interval in the vertical direction. At each point the wire
was rotated 90° electronically so as to not only take the
turbulence intensity measurement but also to check the sym-
metry of the turbulent flow field. Temperature variation
during a scan was kept to a minimum, usually 3°F or less. To
insure repeatability and check effect of temperature the
vertical traverse was done again. In this instance values
at .5 inch increments were taken starting at the outer edge

of the wake.

(8) The slant wire was installed and adjusted to lie in vertical plane. Data was taken in the same manner as step (7) except the wire was rotated 180° in both the vertical and horizontal planes.

4. DATA REDUCTION

4.1 Mean Flow Velocity

The initial task in the data reduction was to determine the mean
flow velocity variations using the pressure measurements. The mean
total pressure is defined by

$$P_t = P_s + \rho\frac{v^2}{2} + \rho\frac{\overline{v'^2}}{2},$$

where $v^2 = U^2 + V_T^2 + V_R^2$ (with $V_R^2 = 0$) and $\overline{v'^2} = \overline{u'^2} + \overline{v'^2} + \overline{w'^2}$.
Due to the small contribution of the turbulence in comparison with
the basic mean quantities, the term $\rho\,\overline{v'^2}/2$ was dropped. For both
models #1 and #2 the dynamic pressure, $P_t - P_s$, was measured directly
since there was negligible flow angularity with proper alignment of
the pitot-static tube, and the axial velocities were readily cal-
culated. The density was obtained by using the ideal gas equation of
state, the static pressure was given by

$$P_s = (P_m - P_B)_{LOCAL} + P_B - \frac{1}{2}\rho(\overline{v'^2} + \overline{w'^2}),$$

where P_m and P_s are the measured and actual static pressures, respec-
tively, and the temperature was the average value taken during a
particular test run. All pressure measurements were in inches of
water, except the barrometric pressure which was in millibars.

In the case of model #3 there was flow angularity resulting from

20

the induced swirl. Since the pitch angle of the flow with respect to the free stream direction was less than 1°, the axial and tangential velocity components were deduced from

$$U = V \cos \psi, \quad V_T = V \sin \psi,$$

where ψ is the yaw angle determined from the directional probe. Flow yaw angle variations were obtained using the calibration curve $\Delta P/(P_t - P_s)$ versus ψ (Fig. 9). The pressure difference was normalized by the local Q.

4.2 Turbulence Quantities

In order to simplify hot wire data reduction considerably the following assumptions were made: Constant temperature in the flow, constant fluid properties, ideal operation of the hot wire by the electronic circuit. Since the mean velocity U was much greater than the turbulent velocities for these experiments, the turbulence intensities were readily calculated using a calibration curve of E versus U (Ref. 24). For example

$$\sqrt{u'^2} = \frac{e_1 + e_2}{dE/dU},$$

where dE/dU is the slope corresponding to (U, E_M) and e is the RMS reading. E_M is the mean (D.C.) voltage reading for the hot wire.

To calculate the remaining turbulent intensities (radial and tangential) and the turbulent shear stresses an additional calibration

curve was required, namely E versus θ, where θ is the angle of attack of the wire. Two equations, one for +45° (the inclination of the slant wire with respect to the free stream direction) and the other for -45°, were added or subtracted and the resulting equations were solved for the desired intensity or shear stress. For example,

$$(e)_{\theta=\pm45°} = \left(\frac{dE}{dU}\right)^2_{\theta=\pm45°} \overline{u'^2} + 2\left(\frac{dE}{dU}\right)_{\theta=\pm45°}\left(\frac{dE}{d\theta}\right)_{\theta=\pm45°} \overline{u'v'} + \left(\frac{dE}{d\theta}\right)^2_{\theta=\pm45°}\overline{v'^2},$$

Ref. 23. For details concerning the turbulence data reduction see Ref. 24.

5.   EXPERIMENTAL RESULTS

5.1 Wind Tunnel Flow

In any experimental fluid dynamics investigation it is of para-
mount importance to establish the quality of the flow under considera-
tion. Since the wind tunnel used here has interchangeable test
sections, the walls required fine adjustment in alignment before test-
ing whenever sections were changed. After these adjustments were made,
the flow angularity in the vertical plane was less than -1°; the effect
on measurements was considered negligible. The free-stream angularity
in the yaw direction (lateral plane) was also less than -1°. For these
experiments the flow was essentially uniform across the test section,
a maximum 2% deviation from the centerline value, without the presence
of the model, and the turbulence level of 1.08 is one of lowest of the
existing wind tunnels in the use today. The axial pressure gradient
was found to be essentially zero for the major part of the working test
section. In addition, due to the significance in flow symmetry, both
in magnitude of experimental effort and analysis, extensive checks on
the symmetry of the profiles of all models tested with respect to
peripheral angle were made. The maximum errors in dynamic pressure
in the lower two quadrants (opposite the strut) were generally less
than ±2%.

5.2 Drag Body Model

Model #1, a drag body, was studied not only to provide a reference
comparison case for the self-propelled bodies but also to document the

wake flow of a slender, axisymmetric body in a high Reynolds number flow. Using equation (1) of Ref. 10, which includes the contribution of turbulent fluctuations, the average drag coefficient C_D was calculated to be .0919. The variation of C_D with axial position is shown in Fig. 10; there is a maximum deviation of 15%. Since only five stations were examined, the energy conservation equation, Ref. 11, in integral form could not be evaluated totally. That is, the contribution due to axial variation was estimated, and the axial distribution of all contributing integrals is given in Ref. 24, which contains all of the turbulence measurements of this effort. Note, due to self-preservation, theory predicts that each of these integrals should be constant with X/D.

Mean velocity distributions for stations X/D = 2, 5, 10, 20, and 40 at the nominal free stream dynamic pressure of 9.5 inches of H_2O are provided in non-dimensional form in Fig. 13, and a complete listing of the data is given in Tables 1-5 in Appendix D. They represent typical elementary shear flow profiles; that is, the velocity deficit spreads outward and decreases on the centerline as the flow proceeds downstream. Static pressure graphs in the form $(P_s-P_B)/Q_E$ versus R/R_o, Fig. 15, show essentially constant radial variation, and the small values of (P_s-P_B) indicate a nearly zero axial pressure gradient. Even though the principle thrust here was at a nominal speed of 206 ft/sec, it is interesting to note the U/U_E distributions for 101 ft/sec shown in Fig. 11. A comparison of these two flows reveals the expected increase in centerline velocity deficit for the higher speed,

a direct consequence of the greater retarding force exerted by the body on the fluid. The rates of growth of these two wakes, as reflected by $R_{1/2}/R_o$ versus X/D in Fig. 17 ($R_{1/2}$ is the R corresponding to $U = 1/2 \, (U_C + U_E)$), are very similar. However, the wake associated with the higher speed appears to grow a little faster. Self-similarity for both cases is indicated in Figs. 12 and 14, even for $X/D = 2$. In Fig. 17 the axial mean flow velocity deficit decay for $Q_\infty = 9.5$ inches of H_2O is compared with the data for model #1 with $Q_\infty = 2.4$ inches of H_2O, Ref. (10), and Ref. (13). Although the present model centerline values for the $U_\infty = 206$ ft/sec case are higher than those for the $U_\infty = 101$ ft/sec case, the decay rates are essentially the same. Chevray's data for fluid motion about a 6 to 1 oblate spheroid with a $Re_D = 2.75 \times 10^6$, as compared to 6.18×10^5 for this model, reveals a greater rate of decay, while the data from Ref. (13) for a slender, axisymmetric body and $Re_D = .49 \times 10^5$ agrees extremely well with present measurements. The downstream decay of the wake is further characterized by the decrease in turbulence intensity and Reynolds shearing stress with X/D, as demonstrated in Figs. 34 and 19, respectively. Theory predicts that the highest values of these stresses is in the near wake region (region of greatest turbulence production); however, the values obtained for $X/D = 2$ in this experiment are lower than expected.

5.3 Self-Propelled Configurations

In the case of the self-propelled bodies a primary consideration was the simulated zero net-momentum condition. Since the basic

operating conditions for both models were determined at X/D = 5, additional checks were made during testing. The estimated jet velocity U_j required to produce a zero change of momentum flux for model #2 was 1.14 U_E. This value reflects the nature of the experimental set-up used, i.e. a value of U_j = 3.64 U_E was necessary for the disk experiments of Ref. 8. In particular, if the jet had a different diameter or the body was shaped differently, a different jet efflux velocity would be necessary to achieve the momentumless state. The degree to which this condition was realized in the wake flow of model #2 is exhibited in the axial change of C_D (Fig. 10). This shows a maximum C_D for X/D = 5 - 40 of 2.9% of the total drag coefficient of the body. At X/D = 2 the C_D is largest, and there is an 5.3% deficit in thrust required. This is attributed to the close proximity in which measurements were taken and the initial lower temperature of the jet, as compared to the free stream value (buoyancy effects). Another important aspect of the jet, wake flow was symmetry. This was affected by not only the degree of non-uniformity in the free-stream but also that of the air flow at the injection exit, which is indicated in Fig. 20. It is clearly observed from this that the injected flow was not completely uniform; however, the maximum deviation from the zero degree velocity is less than 2%. One reason for the non-uniformity is that the model was not sufficiently long for the flow leaving the plenum chamber to become completely uniform. Also, the flow was affected by vanes, marked I-IV on the graph, required to position the tail. At any rate, the most pronounced effect on the wake resulted from the tail itself, as reflected in the mean flow measurements.

Mean flow velocity profiles at X/D=2, 5, 10, 20, and 40 with Q=9.5

inches of H_2O are shown in Fig. 21. These distributions are based on

the average values obtained in the horizontal and vertical pressure

scans since the operating injection pressure was defined that way due

to the slight asymmetry in the injected flow and its corresponding

effect on the total asymmetry of the wake flow. Because of the presence

of the center body in the injection region, there is a velocity defect

in the immediate vicinity of the centerline at stations X/D = 2 and 5.

Beyond the initial wake region, the velocity profiles resemble those

of a combined jet and wake flow if there were no center body. That

is, there is a velocity excess region in the inner portion of the wake

and a velocity deficit region in the outer part. As a direct con-

sequence of the center body, self-similarity profiles in the usual sense,

$(U-U_E)/(U_C-U_E)$ versus $R/R_{1/2}$, were not possible at all stations. In

particular, the gross effects of the pointed stern such as low center-

line velocity and tail and vane boundary layer wake interaction excluded

the near wake positions X/D = 2 and 5. Although some effects, not

detailed memory of the body, were retained at stations downstream of

X/D = 5, a self-similar nature is observed in the far wake flow. As

in the drag body case the axial pressure gradient was essentially zero;

static pressure profiles are given in Fig. 22. The centerline velocity

excess change with X/D was calculated; this indicated a steady increase

in excess from X/D = 5 to X/D = 10. Moreover, this was felt to be

inadequate for comparison purposes to describe the entire shear flow

development. The axial decrease based upon $(U-U_E)_{max}$ was discerned

to be more definitive (Fig. 23). Like model #1 the asymptotic flow

condition has not been realized within the region tested.

In Tables 6-10 in Appendix D all mean flow data is documented.

The X/D variation of axial turbulence intensity and radial shearing

stress are provided in Fig. 24; this will be discussed shortly

following a description of the mean flow results of model #3.

The degree of the momentumless condition for the propeller-

driven model is depicted in Fig. 10. For positions X/D = 5 and 10

there was an excess thrust of less than 6%, while stations X/D = 20

and 40 showed a slight drag with a maximum C_D of less than 10% of

the actual C_D of the body. The measurements at X/D = 2 indicated

an excess thrust of about 20%, but there are significant measure-

ment problems at this station due to the large velocity gradients

and high turbulence level. Overall, these results are judged to show

an essentially self-propelled condition.

The dip in static pressure near the axis of the wake for the

downstream positions X/D = 2 and 5 is evident in the profiles in

Fig. 29; there was practically no change in the radial direction

for the established wake flow regime (X/D = 10, 20, and 40). At X/D =

2 there was not only the induced swirl effect but also the disturbance

due to the vortex sheet created by the sheading vortices of the

propeller blade tips. It should be noted that the frequency of

this disturbance was not excluded from the turbulence signal by

a low frequency filter. Moreover, the axial static pressure was

essentially constant as in the other models.

Non-dimensionalized axial velocity profiles for the five stations mentioned previously are given for the propeller-driven model in Fig. 25. The basic character of momentumless wakes is exhibited in these velocity variations, i.e. a velocity defect region and a velocity excess region. However, the velocity excess region is in the outer part of the shear flow, which is contrary to the jet-propelled case. The downstream change in profile shape that occurred in the drag body wake (bell shape maintained through wake development) is not seen in the wake of this model. Moreover, the evolution of the present wake resembles that of the far wake of model #2. This means that the excess and defect regions diminish with X/D. Axial self-similarity velocity profiles for model #3 in Fig. 26 show that there was very good similarity in the inner radial regions; however, the velocity excess region data was not as good. The flow angularity in the yaw direction produced by the propeller is indicated in Fig. 27. These measurements show that there was a maximum deviation of 5.26° from the free stream flow. The swirl velocity distributions, cast in self-similar form in Fig. 28, were determined from these angles. Since the undisturbed flow angularity was not zero, a maximum of -.78°, the curves do not pass exactly through zero at R = 0 inches. Also, due to the very small angles measured beyond X/D = 10 and the corresponding inaccuracy of such measurements, only stations X/D = 2, 5, and 10 are included. The profiles display a solid body of rotation behavior ($V_T \sim R$) in the inner region and decay to approximately zero in the outer region. All data for these mean flow velocity distributions are given in Tables 11-15 in Appendix D.

In Fig. 30 (a log-log graph) the axial centerline velocity deficit decay was found to be linear with a decay rate of $(X/D)^{-.969}$. Although the major part of the momentum transferred by the propeller to the fluid was in the outer portion of the wake for this model, the downstream rate of decrease of $\left|(U_E - U)_{max}/U_E\right|$ compares favorably with data from Ref. 9, where the momentum transfer was confined primarily to the center wake region. The difference is attributed to the higher pitch of the present propeller and its extension beyond the boundary layer of the body. A comparison of the decay rate for this model with that of model #1 shows that the initial decay is faster for the propeller-driven body than the drag body. However, the rates of decay are essentially the same beyond $X/D = 10$. Also, in this region, the $\left|(U_E - U)_{max}/U_E\right|$ diminishes much more rapidly for the jet-propelled model than the other models. The physical explanation for this is that there is a much stronger interaction of the accelerated and retarded fluid regions for model #2 than for model #3. This interaction is sufficiently weak for model #3 that its mean flow wake behavior is not very different from that of ordinary wakes, where there is only a velocity defect region.

An indication of the downstream decay of the swirl velocity is given in Fig. 32. Even though the accuracy of the $X/D = 20$ value is somewhat in doubt, the rapid drop-off rate still characterizes the flow. Finally, to complete the description of the mean flow of this wake it is interesting to note the rate of growth as depicted in Fig. 33, where $R_{1/2}$ is the R at $1/2(\sqrt{\overline{u'^2}})_{max}$ (axial turbulence

intensity). As in the case of the jet-propelled body, the expected straight line variation (on log-log scales) of the wake spreading is not observed in the early portion of the wake. Although the wake continuously grows in the streamwise direction, the initial rate of spreading is higher than the rate further downstream, which is quite different from the single power law growth exhibited by ordinary wakes. The development rate for this model appears to be smaller than the one for model #2, which is also shown in this figure.

Certain representative features of the turbulence such as X/D decay of axial turbulence intensity and Reynolds shearing stresses enhance understanding of the interrelationship between the mean and turbulent motions (i.e. $\overline{-u'v'} = \varepsilon \; \partial U/\partial R$, where ε is the eddy viscosity). The decrease in $(\sqrt{\overline{u'^2}})_{max}/U_E$ with increasing X/D is presented for all three models in Fig. 34. The turbulence intensity at corresponding stations was greater for model #2 than model #3, a result of the different propulsion mechanisms; however, the streamwise decay rate was greater for the propeller-driven case. Fig. 31 gives the axial variation of the maximum value of the principal Reynolds stress. In this instance, the decay is more rapid for model #2 than model #3, and the values for model #3 are greater beyond $X/D = 2$ than the absolute value of those for model #2. The magnitude of the wake flow shearing action of model #1 is greater than that of the propeller-driven body and less than that of the jet-propelled body.

6. COMPARISON OF EXPERIMENTS WITH NUMERICAL CALCULATIONS

As mentioned previously, numerical computations were made to pre-
dict and to compare with present experimental results the downstream
decay of wakes as reflected by the streamwise variation of centerline
mean velocity deficit and radial Reynolds shearing stress. The numeri-
cal values were determined from present initial station experimental
data supplied to a turbulent kinetic energy computer program provided
by Philip Harsha (Ref. 19). This is a versatile program that was de-
signed to handle a wide range of free-turbulent mixing problems, i.e.
both 2-D and axisymmetric jets and wakes. The procedure used was
obtained from the turbulent kinetic energy (TKE) method described in
Ref. 20. For the fluids problems investigated here the following basic
assumptions were made: 1) The mixing field is in a constant pressure
environment uninfluenced by wall effects; 2) Gradients with respect
to the radial direction R are very much greater than those with respect
to the axial direction X (allowing a set of parabolic partial dif-
ferential equations to be solved, including continuity, momentum, and
turbulent kinetic energy; 3) Gradient diffusion model applicable;
4) Constant eddy viscosity across the wake; this can be replaced with
a distribution if available. Besides the basic equations an additional
relationship was required in order to have a self-contained system.
Namely, a relation between the turbulent shear stress τ and the tur-
bulent kinetic energy k was necessary. In this approach the relation

$$\tau = a_1 \rho k$$

was used. Although a_1 was taken as a constant value of .3 over most of the wake flow, it is not a constant in the vicinity of the centerline since the shear stress vanishes for axisymmetric flows. In this program Harsha used

$$a_1 = .3 \frac{\partial U/\partial R}{|\partial U/\partial R|_{max}}$$

for normal shear flows, i.e. model #1. This relation was applied from the centerline to the point $\partial U/\partial R = (\partial U/\partial R)_{max}$, $R = R_{max}$. Beyond $R = R_{max}$

$$a_1 = .3 \frac{\partial U/\partial R}{|\partial U/\partial R|} ,$$

which yields the proper sign. In order to avoid a too high shear stress value in the outer region of the flow for momentumless cases, Harsha modified the program to include the following formulation:

$$a_1 = .3 \frac{\partial U/\partial R}{|\partial U/\partial R|_{max}} \qquad \partial U/\partial R > 0$$

$$a_1 = .3 \frac{\partial U/\partial R}{|(\partial U/\partial R)_{min}|} \qquad \partial U/\partial R < 0$$

Complete information on modeling of the turbulent kinetic energy equation, i.e. dissipation and diffusion terms, is provided in Ref. 19. Note, all parameters involved in modeling were taken as the normal values, as dictated by previous experiments. This was necessary since the present effort did not penetrate the regime of statistical

flow characteristics, i.e. turbulence length scale, auto-correlation

functions, energy spectrum. Even so, predictions of the decay of mean,

axial velocity def'cit or excess and shear stress were fairly good.

Since this formulation is parabolic, the principal information re-

quired to undertake a calculation is in the form of initial conditions.

These were taken from the experimental measurements at $X/D = 2$. This

included not only the radial distributions of the dependent variables,

but also an initial eddy viscosity distribution which was obtained from

the measured shear stress and velocity distributions. For model #2,

this procedure produced results in disagreement with the data, so an

alternate calculation using a constant eddy viscosity of 0.072 suggested

by Naudascher's data was attempted. These are the calculations shown

in Figs. 23 and 24.

This computer routine did not include a tangential momentum equa-

tion, so that swirl is not accounted for and the calculations for model

#3 are not exact and must be interpreted carefully. The principal cal-

culations were begun at $X/D = 5$, since the swirl velocity has decayed

to a low value at that station. It is significant, however, that cal-

culations begun at $X/D = 10$ and 20 showed the same trends even though

the swirl velocity had decayed to much lower values by those stations.

For model #1 the numerical prediction of the downstream decay of

the centerline mean velocity deficit, as shown in Fig. 18, agrees

fairly well with the experimental results. Even though the actual

values are slightly underestimated (maximum of 10%), the rate of decay

is followed very closely. There are probably initial station effects

since agreement with experiment improved by augmenting $(X/D)_i$. More-over, the boundary layer type assumptions made for the theoretical flow model are perhaps not strictly valid for the near wake station of $X/D =$ 5. The calculations for model #2 (Fig. 24) demonstrate good agreement with the data. However, there is a tailing-off of the numerical solution in the $X/D = 40$ region; this was caused by the mass entrainment model used. As for model #3, the numerical computations over predict the experimental values initially, and the rate of decrease of velocity deficit is considerably greater than that suggested by the data when $X/D = 40$ is reached (Fig. 31). Besides the near station and entrain-ment model effects, a part of the reason probably lies in the lack of statistical turbulence data for this kind of flow.

The TKE program also provided the streamwise variation in radial shear stress for each of the models. The computations for models #1 and #3, as depicted in Figs. 19 and 32, respectively, show fairly good agreement with experiment; however, the rates of decay are lower than they should be. In the case of model #2, the trend shown follows that exhibited by the experiment, but the actual values are underpredicted.

CONCLUSIONS

A definitive comparison of the turbulent wake flows behind

axisymmetric bodies, including self-propelled configurations, has been

accomplished. The data from these experiments provide a stringent

test against which shear flow analyses can be refined. Also, the gross

effects on the mean and turbulent fluid motions (i.e. shape of mean

flow profiles and axial turbulence intensity levels) resulting from

different types of propulsion to produce momentumless wakes have been

clearly shown. Analysis of the data has led to the following con-

clusions:

(1) The mean flow in the turbulent wake behind a slender, axisym-

     metric body tends to exhibit a self-similar character (i.e.

     velocity profiles collapse upon each other by appropriate

     scaling) over the near wake (starting at $X/D = 2$) and far

     wake regions at different free-stream velocities. If the

     axial velocity profiles for the wake of a propeller-driven

     body are self-similar for both the inner and outer regions

     of the wake, the scaling for these two regions must be dif-

     ferent.

(2) The streamwise centerline velocity deficit decay rate is

     essentially the same for streamlined drag bodies, regardless of

     the free-stream velocity (i.e. 45.9 ft/sec (Ref. 13), 101 ft/

     sec, 206 ft/sec). Wake decay in the sense indicated by the

     rate of change of $\left| (U_E - U)_{max}/U_E \right|$ with X/D is more rapid for

36

a jet-propelled body than a propeller-driven body. The decay for drag bodies (model #1) is essentially the same as for propeller-driven bodies (model #3). For model #3 the decrease appears to be linear on a log-log scale and proportional to $(X/D)^{-.969}$.

(3) Drag body wakes and zero net-momentum defect wakes show two distinctly different kinds of spreading. In particular, for self-propelled bodies the initial rate of spreading is higher than the rate further downstream, which is contrary to the single power law growth displayed by conventional wakes.

(4) The structure of the wake of model #3, velocity excess in the inner portion and deficit in the outer region, is more realististic than that observed for the propeller-driven body of Ref. 9. The difference is a direct consequence of the scaling between the propeller and the body boundary layer.

(5) The magnitude of the maximum axial turbulence intensity at corresponding axial stations $(X/D \geq 5)$ is larger for a jet-propelled body than for a propeller-driven body with the same geometry. However, the absolute value of maximum radial shear stress is greater (beyond $X/D = 2$) in the latter case. The rate of $(\sqrt{\overline{u'^2}})_{max}$ decay is noticeably steeper for the propeller-driven body, and the $|(\overline{u'v'})_{max}/U_E^2|$ decay is much more rapid for the jet-propelled case than for the propeller-driven case.

(6) Using typical values of turbulence related quantities (such as turbulent Prandtl number, characteristic length scale used in defining the turbulent Reynolds number, and turbulence length scale) obtained from previous wake flow experiments, the turbulent kinetic energy numerical approach adequately predicts $\left| (U_E - U)_{max}/U_E \right|$ decay for models #1 and #2. The prediction of the radial shear stress decay trends is fairly good for all models.

REFERENCES

1. Schlicting, H., Boundary Layer Theory, McGraw-Hill, New York, 1968.

2. Hinze, J. O., Turbulence-An Introduction to Its Mechanism and Theory, McGraw-Hill, New York, 1959.

3. Schetz, J. A., "Some Studies of the Turbulent Wake Problem," Astronautica Acta, Vol. 16, 1970, pp. 1-11.

4. Schetz, J. A. and Favin, Stanley, "Analysis of Free Turbulent Mixing Flows without a Net Momentum Defect," AIAA Journal, Vol. 10, No. 11, pp. 1524-1526.

5. Ridjanovic, M., "Wake with Zero Change of Momentum Flux," Ph.D. dissertation, 1963, University of Iowa, Iowa City, Iowa.

6. Wang, H., "Flow Behind a Point Source of Turbulence," Ph.D. Dissertation, 1963, University of Iowa, Iowa City, Iowa.

7. Carmody, Thomas, "Establishment of the Wake Behind a Disk," Journal of Basic Engineering - Transactions of the ASME, Dec. 1964, p. 869.

8. Naudascher, Edward, "Flow in the Wake of Self-Propelled Bodies and Related Sources of Turbulence," Journal of Fluid Mechanics, Vol. 22, part 4, 1965, pp. 625-656.

9. Gran, R. L., "An Experiment on the Wake of a Slender Propeller-Driven Body", TRW Systems Group Report for ONR, June 1973.

10. Chevray, R., "The Turbulent Wake of a Body of Revolution," Journal of Basic Engineering-Transactions of the ASME, Series D, 1968, pp. 275-284.

11. Hokenson, G. J. and Schetz, J. A., "Free Turbulent Mixing in Axial Pressure Gradients," Journal of Applied Mechanics, June 1973, pp. 375-379.

12. Bradshaw, P., An Introduction to Turbulence and its Measurement, Pergamon Press, 1971.

13. Bukreev, V. I., Kostomakka, V. A., and Lytkin, Yu, "Axisymmetric Turbulent Wake Behind a Streamlined Body", Siberskae, Otdelinie An SSSR, Instituk Gidrodinamiki, Dinamika Sploshhoi Sredy, No. 10, 1972, pp. 202-207.

14. Bukreev, V. J., Kostomakha, V. A., and Lytkin, Yu, M., "Turbulent Energy Balance in Axisymmetric Wakes Behind Differently Shaped Bodies," Prikladnaya Mikhanika i Tekhnicheskaya Fizeka, No. 1, 1974, pp. 165-168.

15. Bukreev, V. I., Kostomakha, V. A., and Lytkin, Yu, M., "The Influence of Body Shape on the Characteristics of a Self-Similar Axisymmetric Wake," Doklady Akademii Nank SSSR, Vol. 207, No. 4, 1972, pp. 804-807.

16. Cooper, R. D. and Lutzky, M., "Exploratory Investigation of the Turbulent Wakes Behind Bluff Bodies," DTMB R&D Rept. No. 953, Oct. 1955.

17. Hall, A. A. and Hislop, G. S., "Velocity and Temperature Distributions in the Turbulent Wake Behind a Heated Body of Revolution," Proc. Comb. Phil. Soc. 34, 1938, p. 345.

18. Ilizarova, L. I. and Pochkina, K. A., "Experimental Study of a Wake Behind a Body of Revolution," Prom. Aerodynamika, No. 23, 1962.

19. Harsha, Philip T., "A General Analysis of Free Turbulent Mixing", Users Manual (in draft form), ARO, Inc.

20. Harsha, Philip T., "Prediction of Free Turbulent Mixing Using a Turbulent Kinetic Energy Method," in Proceedings of the 1972 NASA-Langley Working Conference on Free Turbulent Mixing, NASA SP-

21. Dommasch, D. O., Elements of Propeller and Hellicopter Aerodynamics, Pitman Aeronautical Publications, Aeronautical Engineering Series, 1953.

22. Durand, W. F. (Editor in Chief), Aerodynamic Theory, Division L - Airplane Propellers by H. Glauert, Dover Publications, 1963, pp. 169-310.

23. Tieleman, H. W., "Viscous Region of Turbulent Boundary Layer," Colorado State University, Tech. Rept. CER 67-68HWT21, 1967.

24. Chieng, C. C., Ph.D. Thesis, Aerospace and Ocean Engrg. Dept., VPI & SU, October 1974, also to be published as VPI-Aero-016 by C. C. Chieng, A. K. Jakubowski, and J. A. Schetz.

25. Ginevskii, A. S., Pochkina, K. A., and Ukhanova, L. N., "Propagation of Turbulent Jet Flow with Zero Excess Momentum", Fluid Dynamics Academy of Sciences USSR, Vol. 1, No. 6, November-December 1966, Faraday Press, Inc.

26. Buckinskaya, E. K. and Pochkina, K. A., "Investigation of Vortex Wake Behind a Body of Revolution, Prom. Aerodynamika No. 23, 1962.

APPENDIX A

DISCUSSION OF PROPELLER

APPENDIX A

The plastic, 6 inch diameter model airplane propeller used as a propulsive mechanism for model #3 was tested in the VPI & SU 3 ft. subsonic wind tunnel. This tunnel is an open-throat return type with a circular cross-section and a speed range of 0-147 ft./sec. The .1875 inch diameter propeller shaft was rotated by a .5 horsepower Westinghourse Electric Corp. D. C. motor (maximum rpm of 8,800). This motor was fitted inside a 19 inch long axisymmetric body with a wooden nose, a 11.125 inch long steel cylindrical middle section, and a wooden tear drop shaped stern. Also, the motor was connected to a strut that was part of the tunnel balance system. This four-component system permits measurement of lift and drag forces and pitching and rolling moments. The strut is the only part of the balance apparatus in the airstream. A streamlined shield (3 inch chord and 22.25 inches in height) was welded to the middle section of the body containing the motor, and it was mounted independently of the balance system (minimization of tare drag). Finally, the propeller was located sufficiently far in front of the body ($\approx$ 2.5 inches) so as to minimize propeller induced drag. There was no appreciable bending of the shaft during wind tunnel experiments.

Propeller tests were conducted at the following free stream dynamic pressure settings (in inches of H_2O): .5, 1.0, 1.5, 2.0. For each tunnel Q, the voltage E of the motor was set at different values (2-20) volts), and the corresponding current I, the propeller rpm, and

43

the forward thrust were recorded. A variable power supply unit (max. voltage of 40 volts) was used to drive the motor and indicate the current. The rpm of the propeller was measured with a General Radio Co. Strobatac (Type 1531-AB), the thrust was measured on the drag scale (negative drag). From these measurements the apparent thrust coefficient of the propeller for different values of the advance ratio was calculated. The apparent thrust coefficient is defined by

$$C_T = \frac{T}{\rho n^2 D_1^4} \; ,$$

where T is thrust, n is the propeller revolutions per second, and D_1 is the diameter of the propeller disk. Here, the term apparent refers to a thrust value not corrected for propeller induced drag or inter-ference effects. The advance ratio is a measure of the forward distance traversed by the propeller per revolution. When this quantity is non-dimensionalized by the diameter D_1, it is called the advance-diameter ratio and is given by

$$J = \frac{V_\infty}{n D_1}$$

Another important aspect of performance is the efficiency η_p of the propeller. This is normally taken as the ratio of output power (or thrust power, TV) to input power (or torque power). Input power P is defined by the product $M\Omega = M 2\pi n$, where M is the torque applied by the motor to the propeller and Ω is the angular velocity. In order to determine P the motor was first fastened to a platform, and a 1 inch

diameter aluminum disk (essentially weightless) was placed on the shaft.
Nylon chord extending from a linear force scale, which was located
above the disk, was wrapped one revolution around the disk and connected
to a tray. The tray was located below the level of the motor and was
used to hold various weights. A series of designated weights were
placed on the tray. For each weight the motor was run at different
voltage settings. The current of the motor and the rpm of the shaft
were measured and recorded as they were in the wind tunnel tests. The
initial and final weights, w_1 and w_2, indicated on the scale were also
recorded. Therefore, the torque developed by the motor, which is given
by

$$M = (w_1 - w_2)R_1 \; ,$$

where R_1 is the radius of the disk, was determined. Since the revolu-
tions of the shaft were also known, the torque power was calculated.
Graphs of P versus n and P versus I were made so that the input power
corresponding to various values of J could be readily obtained.

The performance characteristics of propellers with varying degrees
of blade twist were examined using graphs of C_T versus J and η_p versus
J. Before the blades were twisted, the standard geometric pitch angle
of each propeller was 13.5^o and the experimental mean pitch was 3
inches. The geometric pitch angle B is the angle between the chord
line of a given blade section and a plane taken perpendicular to the
propeller shaft. Since this angle varies from station to station along
the blade, the angle at .7 R, where R is the radial distance from the

center of the propeller hub, is considered standard. The experimental

mean pitch is the advance per revolution at which the thrust of the pro-

peller becomes zero. This is an important aerodynamic parameter

because the corresponding advance-diameter ratio is a direct indication

as to how much the forward speed of the propeller exceeds the rota-

tional, speed. The final propeller selection was based upon estimated

requirements of model #3 (i.e. thrust necessary to balance drag and

required rpm) and the "open water" type propeller tests described pre-

viously in this discussion. In addition, a primary objective was to

have an η_p of about .65. Upon evaluating the performance results

in light of these requirements, a propeller with a chord at .7R of

.563 inches, a standard pitch angle of approximately 52°, and an

experimental mean pitch J_E of 14.76 inches was selected. The solidity

σ_R, ratio of blade area to the swept or disk area ($\frac{Bb}{\pi R}$, where B is the

blade chord), of the propeller was calculated to be .0896.

In Fig. A-1 the variation of C_T with J for the chosen propeller

is shown. As the value of J decreases from the experimental mean value,

C_T increases until it reaches a maximum value of .246 at J = 1.25.

Then there is a slight decrease in C_T, and the static value ($V_\infty = 0$)

reached is .243. The propeller efficiency η_p starts at 0 and increases

with J until the curve peaks (η_p = .805) at approximately J = 1.625

(Fig. A-2). Beyond the peak value the efficiency drops off rapidly

until it becomes 0 at $J = J_E$. In the case of J = 2.04, which is the

operating value for model #3 so that thrust equals drag, the apparent

thrust coefficient and efficiency are .128 and .680, respectively.

However, the C_T corresponding to the measured drag of model #3 is .159,

which exceeds the apparent value by 19.5%. This difference is attributed primarily to the pusher propeller configuration (propeller behind body) used in testing model #3. In particular, previous propeller tests performed in the VPI & SU 3 ft. wind tunnel have indicated that the tractor configuration (propeller in front of body) C_T curve is lower than the corresponding pusher configuration C_T curve.
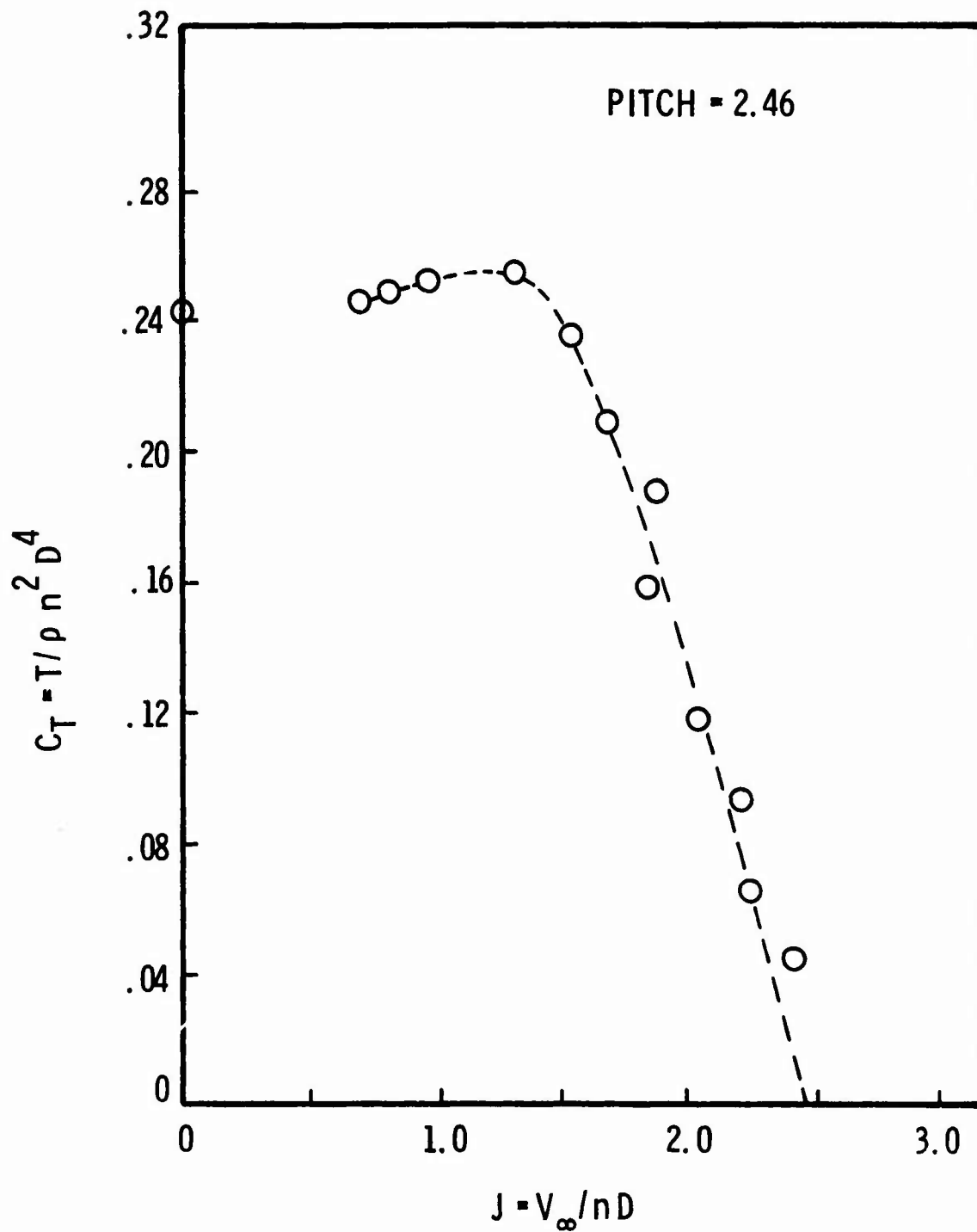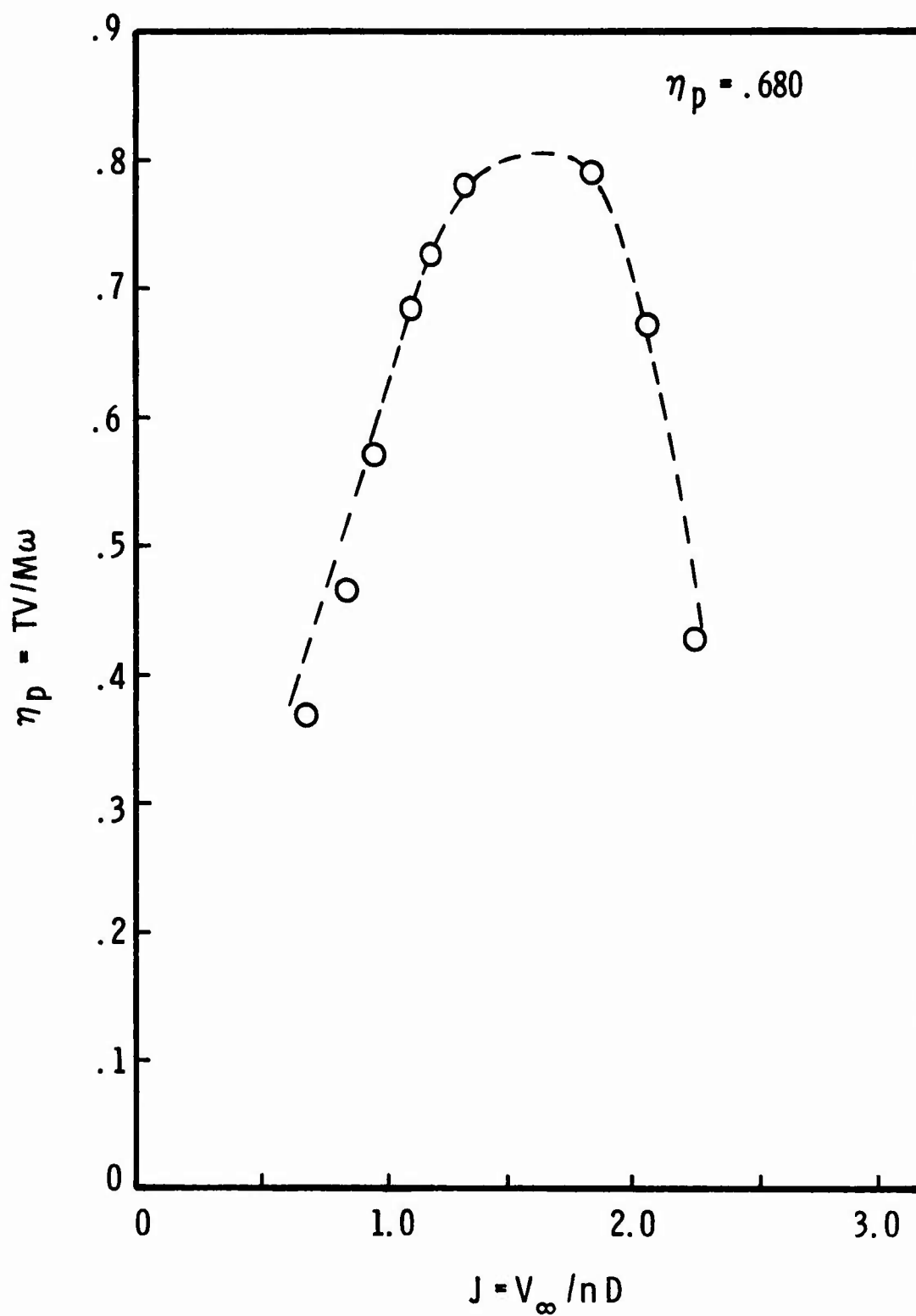
FIG. A-1 THRUST COEFFICIENT VS. ADVANCE RATIO

FIG. A-2   PROPELLER EFFICIENCY VS.   ADVANCE RATIO

APPENDIX B

DISCUSSION OF ERRORS

APPENDIX B

The following discussion presents the sources of error in the measured and computed data. Estimates of these errors and the associated effects are given wherever possible.

Location of probes

Since a 2:1 scaling was used between the recorded position of a given probe and its physical position, the error connected with calibration of the traversing mount was minimized. The maximum probe position error is estimated at $\pm.016$ inches in both the lateral and vertical directions. This does not account for the barely discernible vertical deflection of hot wire probes, which was considered to have a small effect on the turbulence data.

Pressure Measurements

The tunnel dynamic pressure varied slightly during testing; it is estimated that the maximum error is $\pm2\%$. Due to these fluctuations and the turbulence of the flow, the local dynamic pressure exhibited a maximum variation of $\pm1.5\%$. Errors in pressure readings resulting from flow angularity were minimal because of the insensitivity of the pitot-static probe to the small pitch and yaw angles. The use of a Kiel probe in the wake flow of model #3 (a swirling flow) provided extremely accurate stagnation pressure data. Since the maximum yaw and pitch angles with respect to the free-stream flow were less than $+6°$ and $-1°$, respectively, the static pressure measurements taken with the pitot-static probe remained insensitive to the flow angularity.

51

The effect of the turbulence on the pressure measurements is questionable. Although the total pressure measured at a point in a turbulent flow is generally defined by

$$P_t = P_s + \frac{\rho}{2} ((U+u')^2 + v'^2 + w'^2),$$

there have been some calibration tests behind grids of variable ratio of grid-width to space that have indicated smaller values with increasing turbulence level than expected by this formulation. Due to this controversy over the precise effect of the fluctuating components on the stagnation pressure measurement, there have been no corrections made for these experiments.

For this effort the principle influence of the static pressure is found in the momentum balance for the self-propelled bodies. Moreover, errors in the static pressure measurements have a cummulative effect (i.e. the $(P_s - P_B)$ variation is integrated across the shear layer). As mentioned by Wang[6], there is sufficient compensation through the total contribution of the mean velocity (square is proportional to the difference between total and static pressures) in order to give a negligible error in the momentum balance calculation.

Hot Wire Measuremen':

The primary effect on the present hot wire measurements was temperature variation. Since the tunnel was run until nearly an equilibrium temperature was attained, and the time required to take data was minimized, the drift in the RMS readings was reduced sufficiently so

APPENDIX C

(SUBSONIC WIND TUNNEL)

APPENDIX C

Six Foot Subsonic Wind Tunnel

This facility may be classified as a continuous, closed jet, single return, subsonic wind tunnel with interchangeable six-foot round and square test sections. General design features are illustrated in the drawing on the following page. The tunnel is powered by a 600 hp d.c. motor driving a 14 foot propeller providing a maximum speed of 220 feet/ second and a Reynolds' number per foot up to 1.33×10^6. The air stream has a low turbulence factor of 1.08.

The instrumentation available is of a class and variety to permit efficient and accurate detailed studies in nearly all phases of work commonly encountered in wind tunnel practice. The tunnel is equipped with two balance systems. A six-component automatic null balancing machanical system is provided for measuring force and moments on models mounted through the floor or sidewall of the tunnel during static model tests. A six-component electric strain gage balance system is available for use with either static tests or tests during which the model is undergoing steady or oscillatory motion. Both systems feed their output into a readout printing system which allows the operator to read six outputs either from indicator dials or as printed tabulations.

Conventional pressure measuring equipment consisting of manometer banks, survey rakes and boundary layer mice enable detailed pressure and velocity distribution studies to be made. A DISA hot wire system is used to measure fluctuating quantities in turbulent flow.
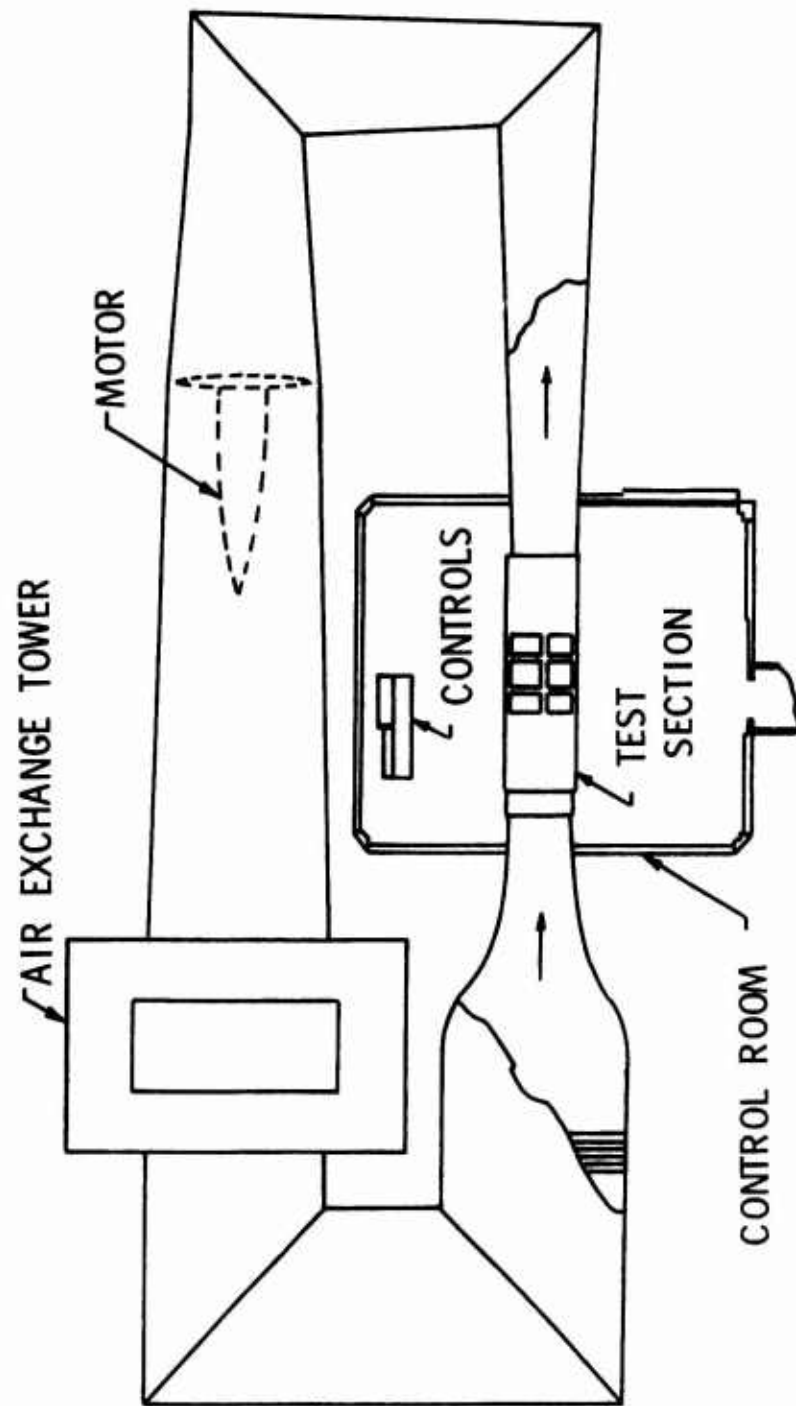
FIG. I   VPI & SU STABILITY WIND TUNNEL

APPENDIX D

TABULARIZED EXPERIMENTAL DATA

TABLE D-1

Drag Body Model (X/D = 2)

$P_B = 1922.40 \frac{lb}{ft^2}$ $T_\infty = 89.7°F$ $U_E = 204.83 \frac{ft}{sec}$ $Q_E = 8.22$ in. H_2O

R/R_o	$(P_s-P_B)/Q_E$	U/U_E
0.0	0.0928	0.533
.083		.561
.167		.633
.25		.711
.333	.0920	.790
.417		.863
.5		.924
.583		.970
.667	.0900	.997
.75		.999
.833		1.0
.917		1.0
1.0	.0876	1.0
1.167		1.0
1.333	.0895	1.0

TABLE D-2

Drag Body Model (X/D = 5)

$P_B = 1928.34 \frac{lb}{ft^2}$ $T_\infty = 89.7°F$ $U_E = 206.92 \frac{ft}{sec}$ $Q_E = 8.24$ in. H_2O

R/R_o	$(P_s - P_B)/Q_E$	U/U_E
0.0	0.0764	0.628
.083		.647
.167		.695
.25		.756
.333	.0755	.820
.417		.881
.5		.934
.583		.975
.667	.0787	.998
.75		1.0
.833		1.0
.917		1.0
1.0	.0804	1.0
1.167		1.0
1.333	.0797	1.0

TABLE D-3

Drag Body Model (X/D = 10)

$P_B = 1924.08 \frac{lb}{ft^2}$ $T_\infty = 99.4°F$ $U_E = 207.29 \frac{ft}{sec}$ $Q_E = 8.28$ in. H_2O

R/R_o	$(P_s - P_B)/Q_E$	U/U_E
0.0	0.0677	0.734
.083		.741
.167		.765
.25		.793
.333	.0685	.830
.417		.867
.5		.906
.583		.942
.667	.0705	.977
.75		.992
.833		.999
.917		1.0
1.0	.0734	1.0
1.167		1.0
1.333	.0747	1.0

TABLE D-4

Drag Body Model (X/D = 20)

$P_B = 1907.14 \frac{lb}{ft^2}$ $T = 96.7°F$ $U_E = 213.03 \frac{ft}{sec}$ $Q_E = 8.71$ in. H_2O

R/R_o	$(P_S-P_B)/Q_E$	U/U_E
0.0	0.0666	0.854
.083		.855
.167		.861
.25		.869
.333	.0662	.879
.417		.892
.5		.906
.583		.925
.667	.0675	.940
.75		.958
.833		.969
.917		.984
1.0	.0712	.990
1.083		.997
1.167		.998
1.25		1.0
1.333	.0723	1.0
1.5		1.0

TABLE D-5

Drag Body Model (X/D = 40)

$P_B = 1895.30 \frac{lb}{ft^2}$ $T_\infty = 94.3°F$ $U_E = 217.10 \frac{ft}{sec}$ $Q_E = 9.03$ in. H_2O

R/R_o	$(P_s-P_B)/Q_E$	U/U_E
0.0	0.0440	0.938
.083		.938
.167		.940
.25		.939
.333	.0434	.942
.417		.945
.5		.947
.583		.951
.667	.0458	.954
.75		.959
.833		.964
.917		.970
1.0	.0464	.975
1.083		.980
1.167		.983
1.25		.988
1.333	.0487	.993
1.417		.996
1.5		.998
1.583		1.0
1.667	.0484	1.0

TABLE D-6

Jet-Propelled Model (X/D = 2)

$P_B = 1916.28 \frac{lb}{ft^2}$ $T_\infty = 58.5°F$ $U_E = 194.58 \frac{ft}{sec}$ $Q_E = 7.91$ in. H_2O

R/R_o	$(P_S - P_B)/Q_E$	U/U_E
0.0	0.1082	0.915
.042		.931
.083		.975
.167		1.074
.25	.1096	1.141
.333		1.146
.417		1.111
.5		1.057
.583	.1103	.990
.667		.942
.75		.920
.833		.938
.917	.1120	.966
1.0		.988
1.083	.1120	.998
1.167		1.0

TABLE D-7

JET-PROPELLED MODEL (X/D = 5)

$P_B = 1903.75 \frac{lb}{ft^2}$ $T_\infty = 52.5°F$ $U_E = 195.35 \frac{ft}{sec}$ $Q_E = 7.95$ in. H_2O

R/R_o	$(P_s - P_B)/Q_E$	U/U_E
0.0	0.0796	1.051
.83		1.063
.167		1.087
.25		1.105
.333	.0798	1.101
.417		1.074
.5		1.035
.583		.998
.667	.0808	.969
.75		.956
.833		.960
.917		.971
1.0	.0820	.984
1.083		.992
1.167		.998
1.333	.0826	1.0
1.5	.0827	1.0

TABLE D-8

Jet Propelled Model (X/D = 10)

$P_B = 1909.57 \frac{lb}{ft^2}$ $T_\infty = 69.8°F$ $U_E = 197.60 \frac{ft}{sec}$ $Q_E = 7.84$ in. H_2O

R/R_o	$(P_s-P_B)/Q_E$	U/U_E
0.0	0.1084	1.082
.083		1.081
.167		1.077
.25		1.070
.33?	.1081	1.056
.417		1.041
.5		1.024
.583		1.006
.667	.1099	.994
.75		.985
.833		.984
.917		.986
1.0	.1121	.990
1.167		.997
1.333	.1126	.999
1.5	.1123	1.0
1.667		1.0

TABLE D-9

Jet-Propelled Body (X/D = 20)

$P_B = 1872.51 \frac{lb}{ft^2}$ $T_\infty = 66.4°F$ $U_E = 203.83 \frac{ft}{sec}$ $Q_E = 8.28$ in. H_2O

R/R_o	$(P_s-P_B)/Q_E$	U/U_E
0.0	0.0820	1.044
.083		1.044
.167		1.041
.25		1.036
.333	.0826	1.032
.417		1.025
.5		1.018
.583		1.012
.667	.0832	1.006
.75		1.003
.833		.997
.917		.997
1.0	.844	.996
1.083		.995
1.167		.996
1.333	.0848	.999
1.5	.0847	1.0
1.667		1.0
2.0	.0851	1.0

TABLE D-10

Jet-Propelled Model (X/D = 40)

$P_B = 1878.68 \frac{lb}{ft^2}$ $T_\infty = 60.7°F$ $U_E = 208.53 \frac{ft}{sec}$ $Q_E = 8.80$ in. H_2O

R/R_o	$(P_s-P_B)/Q_E$	U/U_E
0.0	0.0564	1.008
.083		1.007
.167		1.007
.25		1.006
.333	.0564	1.005
.417		1.004
.5		1.004
.583		1.004
.667	.0570	1.003
.75		1.004
.833		1.004
.917		1.004
1.0	.0570	1.003
1.083		1.004
1.167		1.003
1.333	.0575	1.002
1.5		1.001
1.667	.0580	1.0
2.0	.0575	1.0

TABLE D-11

Propeller-Driven Model (X/D = 2)

$P_B = 1919.46 \frac{lb}{ft^2}$ $T_\infty = 88.1°F$ $U_E = 203.05 \frac{ft}{sec}$ $Q_E = 8.89$ in. H_2O

R/R_o	$(P_s-P_B)/Q_E$	U/U_E	V_T/U_E
0.0	0.0757	0.688	0.0035
.083		.701	.0139
.167	.0757	.733	.0330
.25		.796	.0551
.333	.0732	.860	.0722
.417		.924	.0789
.5	.0794	.989	.0856
.583		1.045	.0765
.667	.0893	1.075	.0680
.75		1.089	.0543
.833	.0881	1.079	.0373
.917		1.045	.0142
1.0	.0960	1.006	-.022
1.083	.0960	1.003	-.052
1.167		1.0	-.0052
1.333	.0993	1.0	-.0050

TABLE D-12

Propeller-Driven Model (X/D = 5)

$P_B = 1926.71 \frac{lb}{ft^2}$ $T_\infty = 100.2°F$ $U_E = 202.35 \frac{ft}{sec}$ $Q_E = 8.81$ in. H_2O

R/R_o	$(P_s-P_B)/Q_E$	U/U_E	V_T/U_E
0.0	0.0980	0.850	0.0069
.083		.852	.0106
.167	.0980	.861	.0167
.25		.879	.0281
.333	.0980	.902	.0429
.417		.934	.0580
.5	.0980	.975	.0647
.583		1.015	.0630
.667	.1043	1.040	.562
.75		1.054	.0496
.833	.1078	1.053	.0400
.917		1.030	.0235
1.0	.1113	1.008	.0099
1.083		1.0	.0013
1.167	.1143	1.0	-.0008
1.25		1.0	-.0017
1.33	.1156	1.0	-.0018

TABLE D-13

Propeller-Driven Model (X/D = 10)

$P_B = 1914.32 \frac{lb}{ft^2}$ $T_\infty = 87.8°F$ $U_E = 203.15 \frac{ft}{sec}$ $Q_E = 8.84$ in. H_2O

R/R_o	$(P_s-P_B)/Q_E$	U/U_E	V_T/U_E
0.0	0.0845	0.943	0.0013
.083		.947	.0049
.167	.0845	.954	.0068
.25		.957	.0087
.333	.0845	.961	.0118
.417		.964	.0160
.5	.0845	.969	.0218
.583		.977	.0269
.667	.0857	.989	.0308
.75		1.0	.0324
.833	.0857	1.009	.0338
.917		1.019	.0333
1.0	.0870	1.023	.0316
1.083		1.023	.0284
1.167		1.015	.0257
1.25		1.009	.0193
1.333	.0910	1.007	.0146
1.5		1.001	.001
1.667	.0932	1.0	.001

TABLE D-14

Propeller-Driven Model (X/D = 20)

$P_B = 1912.37 \frac{lb}{ft^2}$ $T_\infty = 106.5°F$ $U_E = 213.35 \frac{ft}{sec}$ $Q_E = 8.61$ in. H_2O

R/R_o	$(P_S-P_B)/Q_E$	U/U_E	V_T/U_E
0.0	0.0790	0.973	-0.0139
.083		.973	- .0086
.167	.0790	.975	- .0048
.25		.975	- .0022
.333	.0790	.977	- .0002
.5		.984	.0021
.667	.0790	.990	.0024
.833		.994	.0020
1.0	.0813	.997	.0015
1.167		1.0	- .0002
1.333	.0819	1.001	- .0029
1.5		1.001	- .0066
1.667	.0836	1.001	- .0086
2.0	.0848	1.0	- .0120
2.333	.0848	1.0	- .0137

TABLE D-15

PROPELLER-DRIVEN MODEL (X/D = 40)

$P_B = 1917.89 \frac{lb}{ft^2}$ $T_\infty = 87.2°F$ $U_E = 214.07 \frac{ft}{sec}$ $Q_E = 9.00$ in. H_2O

R/R_o	$(P_s - P_B)/Q_E$	U/U_E	V_T/U_E
0.0	0.0533	0.985	-0.0134
.083		.986	- .0124
.167	.0533	.987	- .0111
.25		.988	- .0097
.333	.0533	.988	- .0088
.417		.988	- .0079
.5	.0533	.991	- .0068
.583		.991	- .0055
.667	.0533	.994	- .0044
.75		.994	- .0035
.833	.0533	.997	- .0029
.917		.997	- .0023
1.0	.0533	.997	- .0025
1.167		.998	- .0028
1.333		.999	- .0038
1.5		.999	- .0059
1.667	.0544	1.001	- .0076
1.833		1.0	- .009
2.0	.0555	1.0	- .0101
2.667		1.0	- .0130
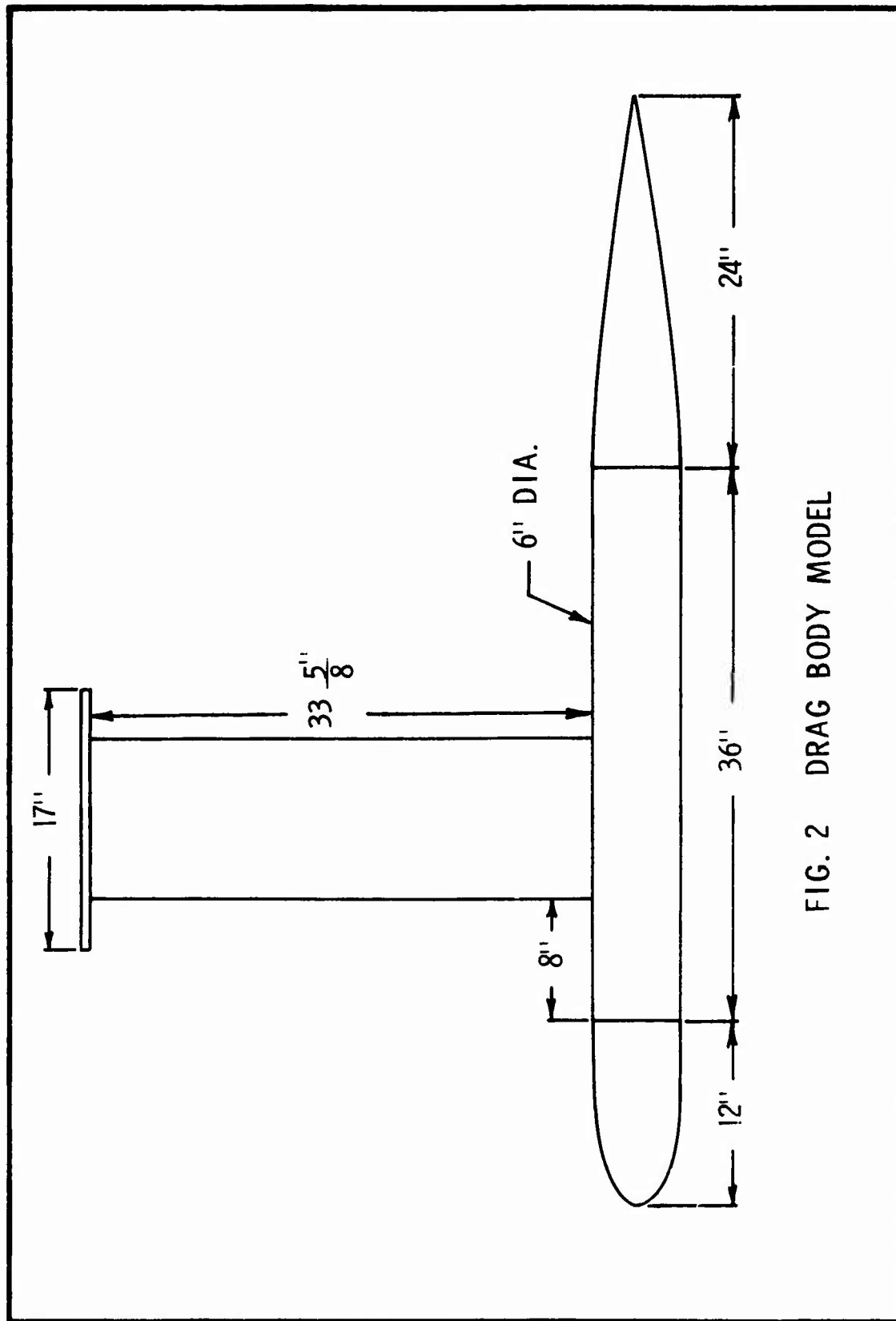
FIG. 2   DRAG BODY MODEL

FIG. 3   PHOTOGRAPH OF JET-PROPELLED MODEL

74

SCREENS

INJECTION HOLES

CHORD $9\frac{1}{2}$"

$33\frac{3}{16}$"

$\frac{3}{8}$"

$13\frac{5}{16}$"

5"

9"

20"

$8\frac{11}{16}$"

6" DIA.

12"
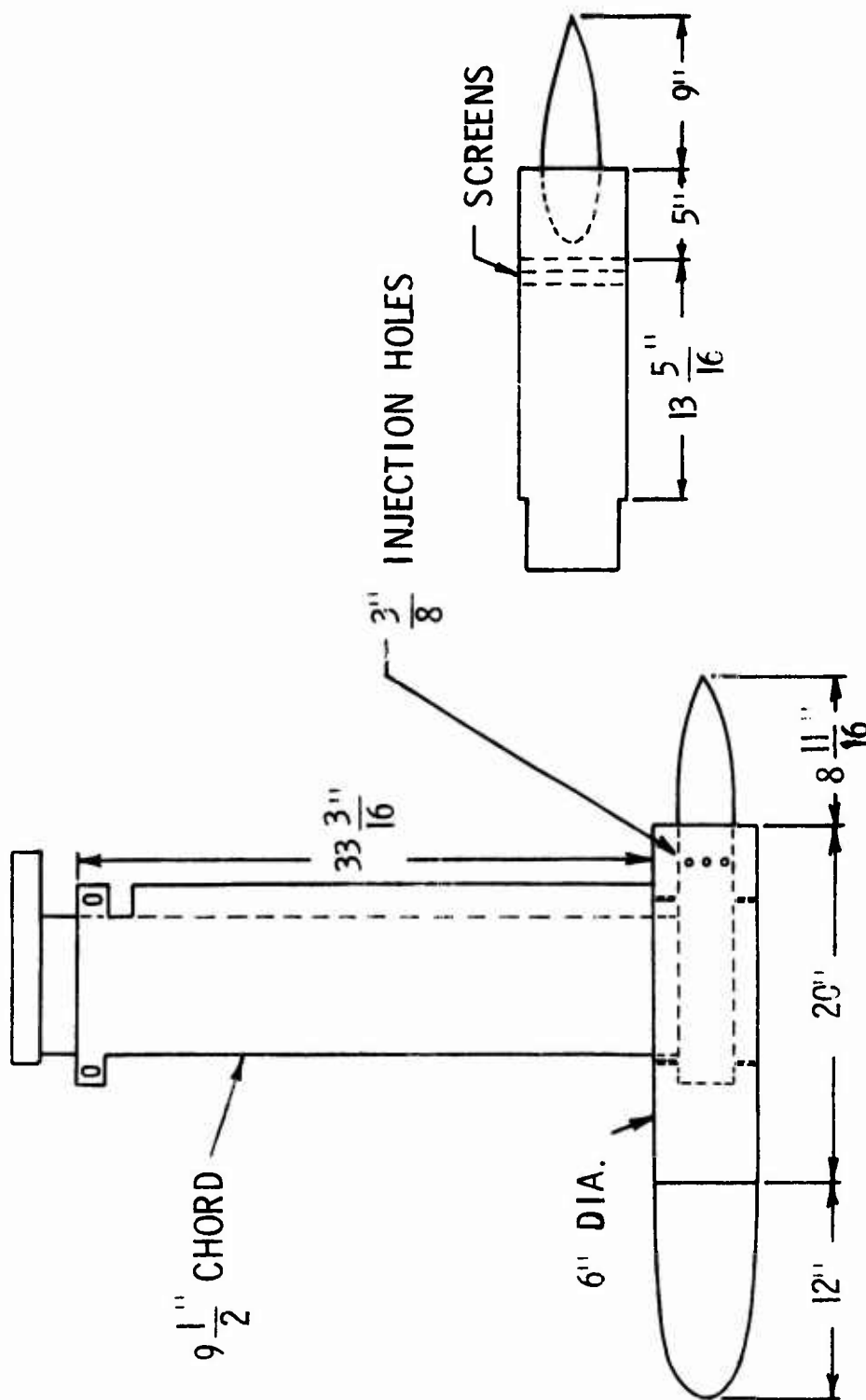
FIG. 4   JET-PROPELLED MODEL
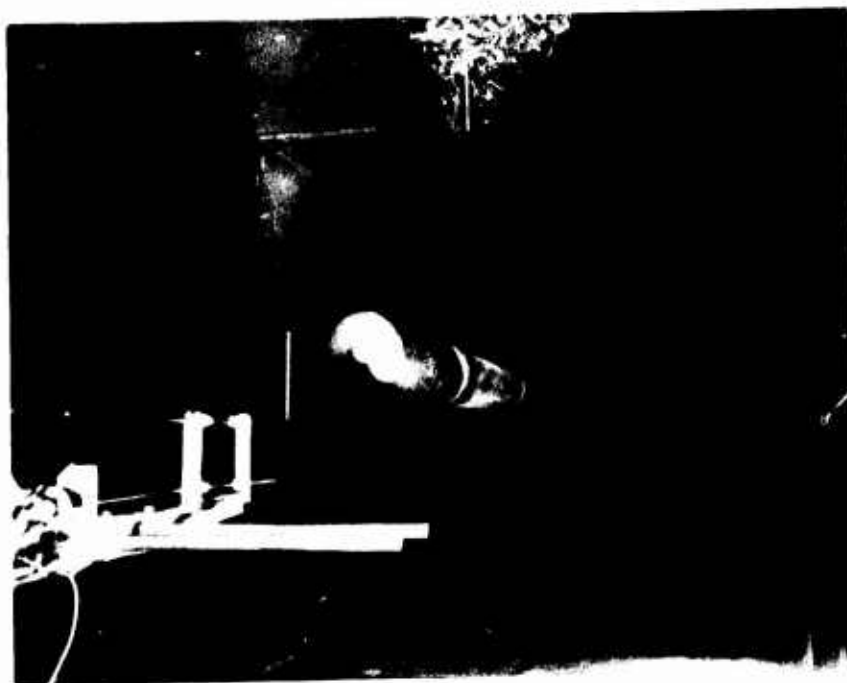
FIG. 5   PHOTOGRAPH OF PROPELLER-DRIVEN MODEL

FIG. 6   AUTOMATIC TRAVERSE

MOUNTING CHUCK

REINFORCING TUBE

1/4"

30°

15"

3/32"

3/8"

2 1/2"

FIG. 7   PITOT-STATIC PROBE

FLOW DIRECTION

REINFORCEMENT TUBE

MOUNTING CHUCKS (BRASS)

18"

1/4"

1/2"

FIN

3/16"

4 1/2"
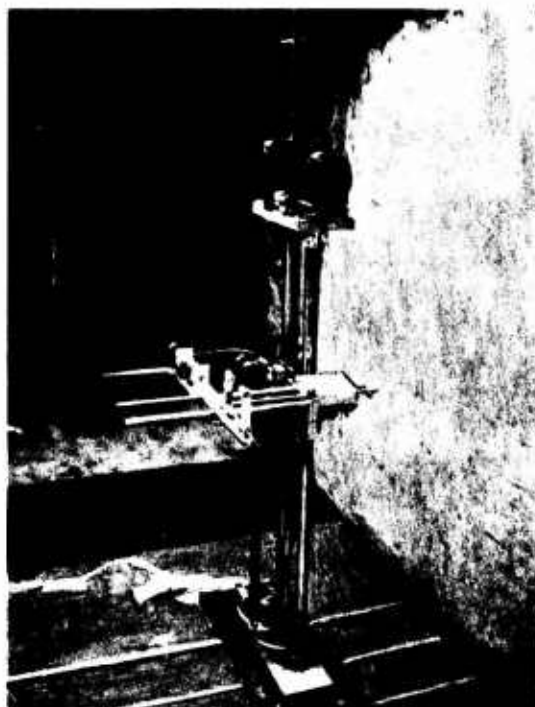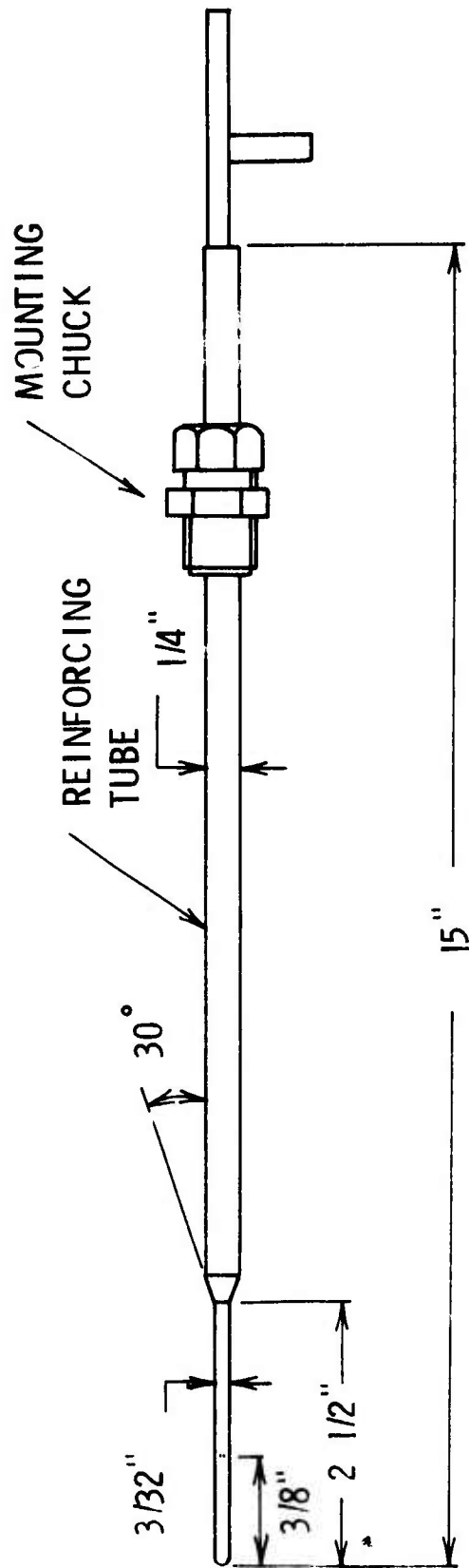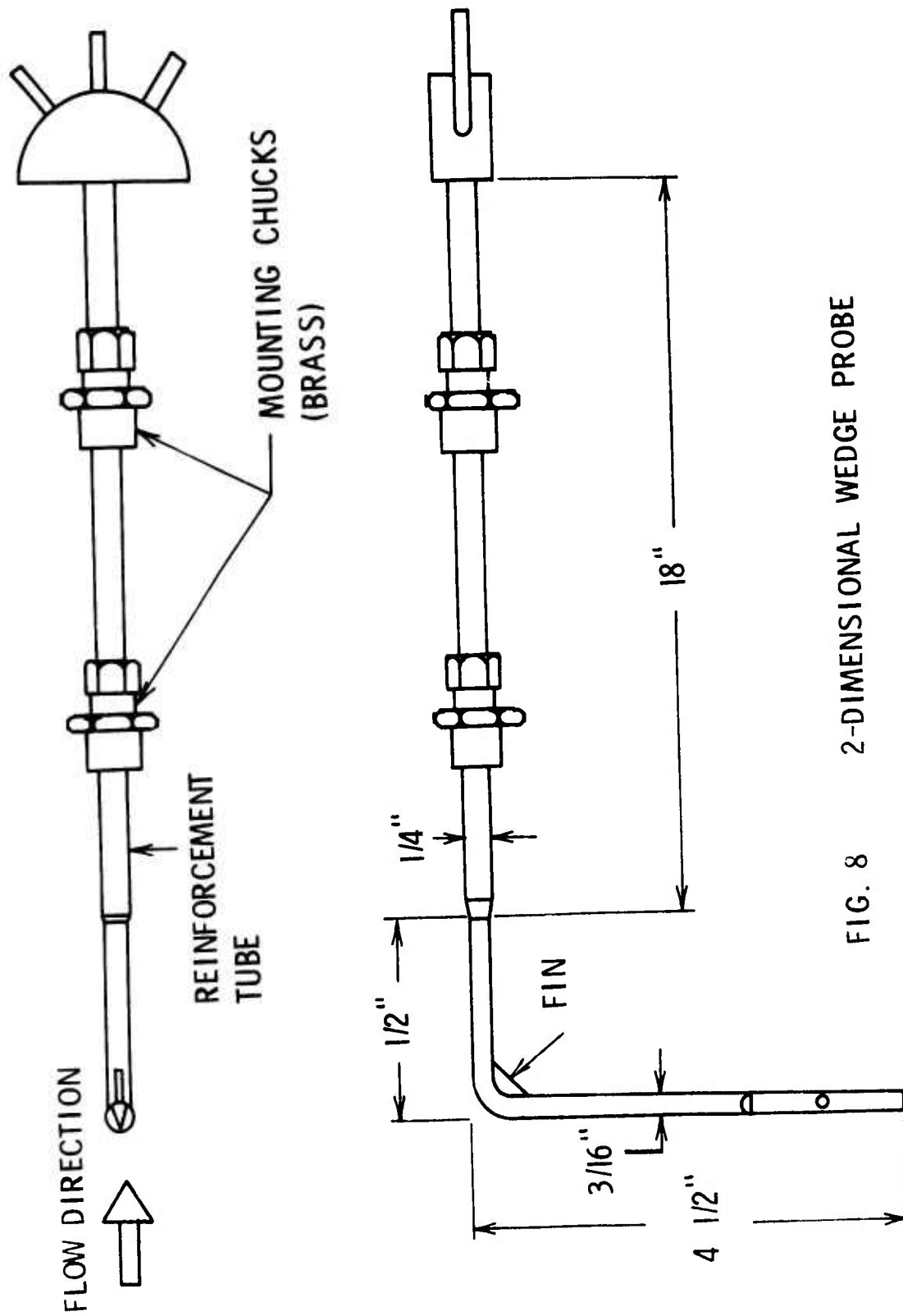
FIG. 8   2-DIMENSIONAL WEDGE PROBE
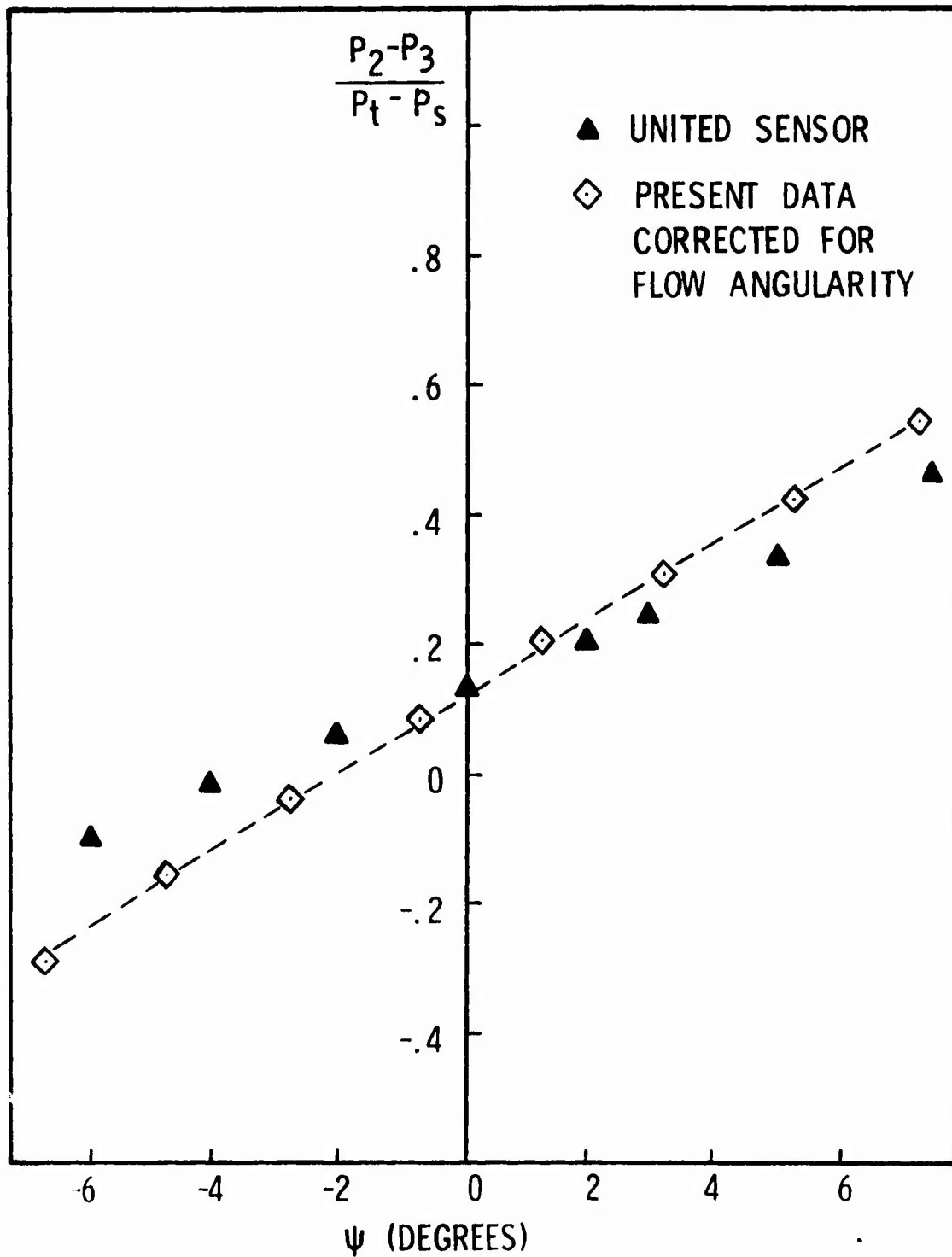
FIG. 9 CALIBRATION OF 2-D WEDGE PROBE
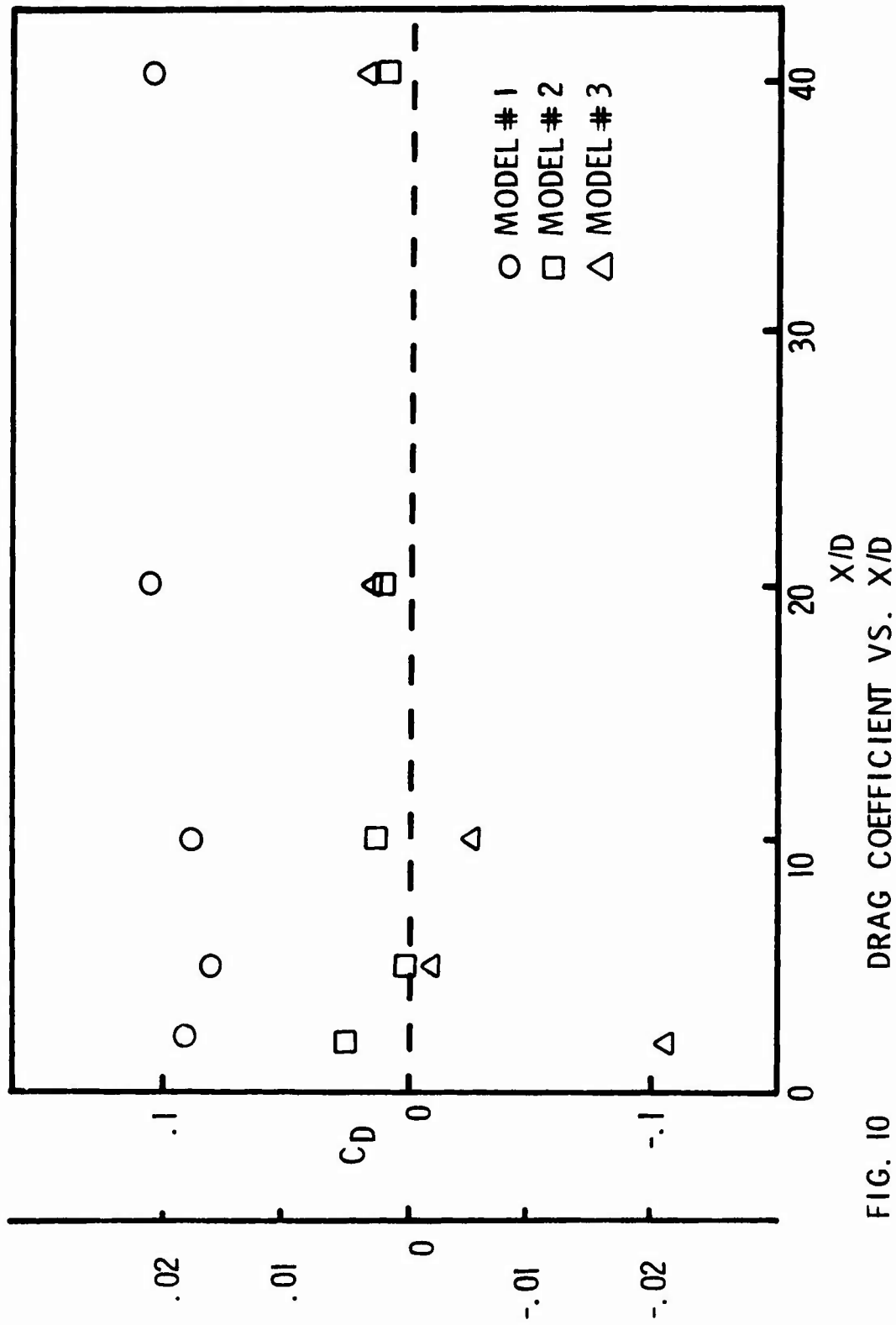
FIG. 10   DRAG COEFFICIENT VS. X/D
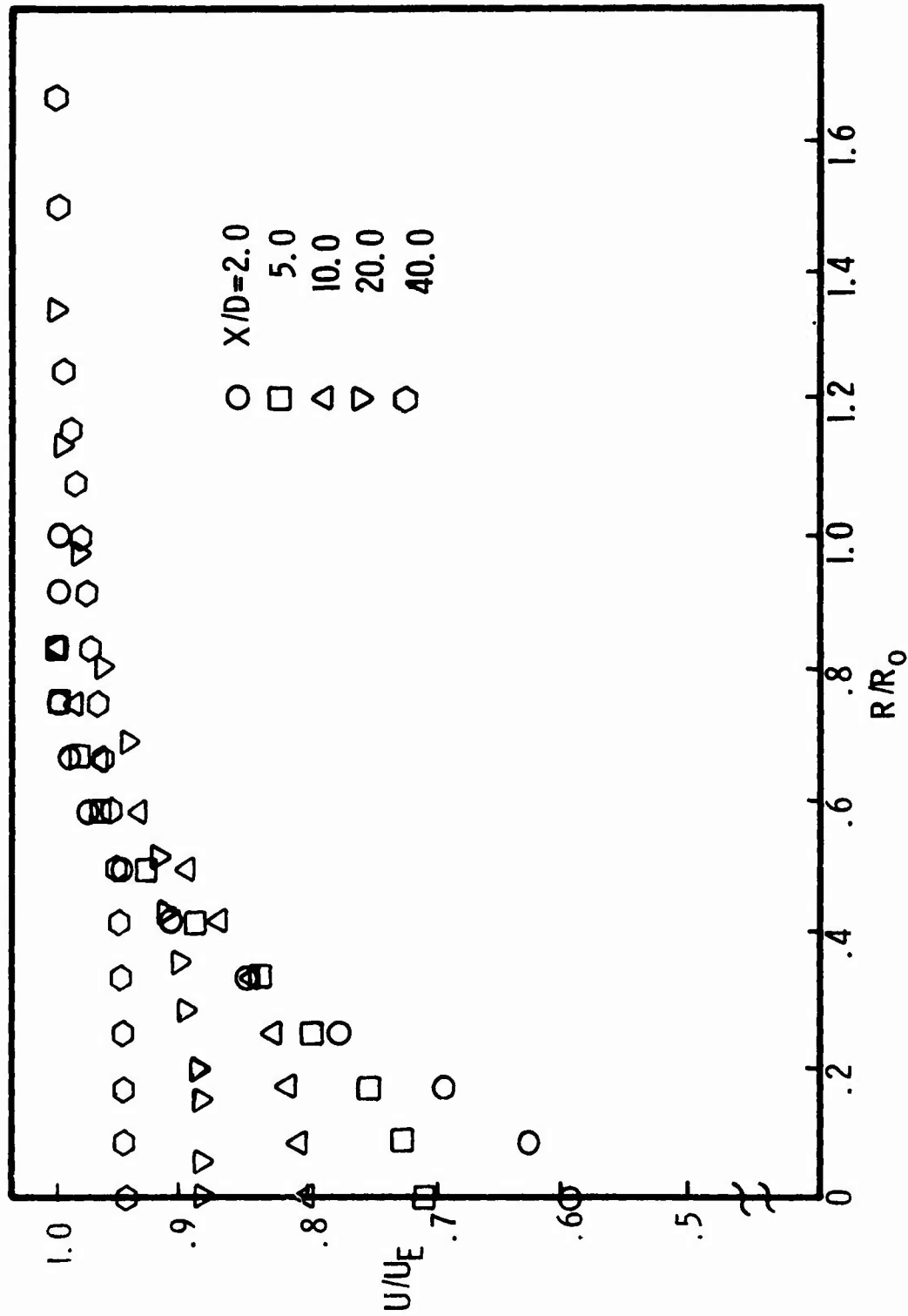
FIG. II   MEAN AXIAL VELOCITY PROFILES FOR MODEL # I ($V_\infty = 101$ ft/sec)
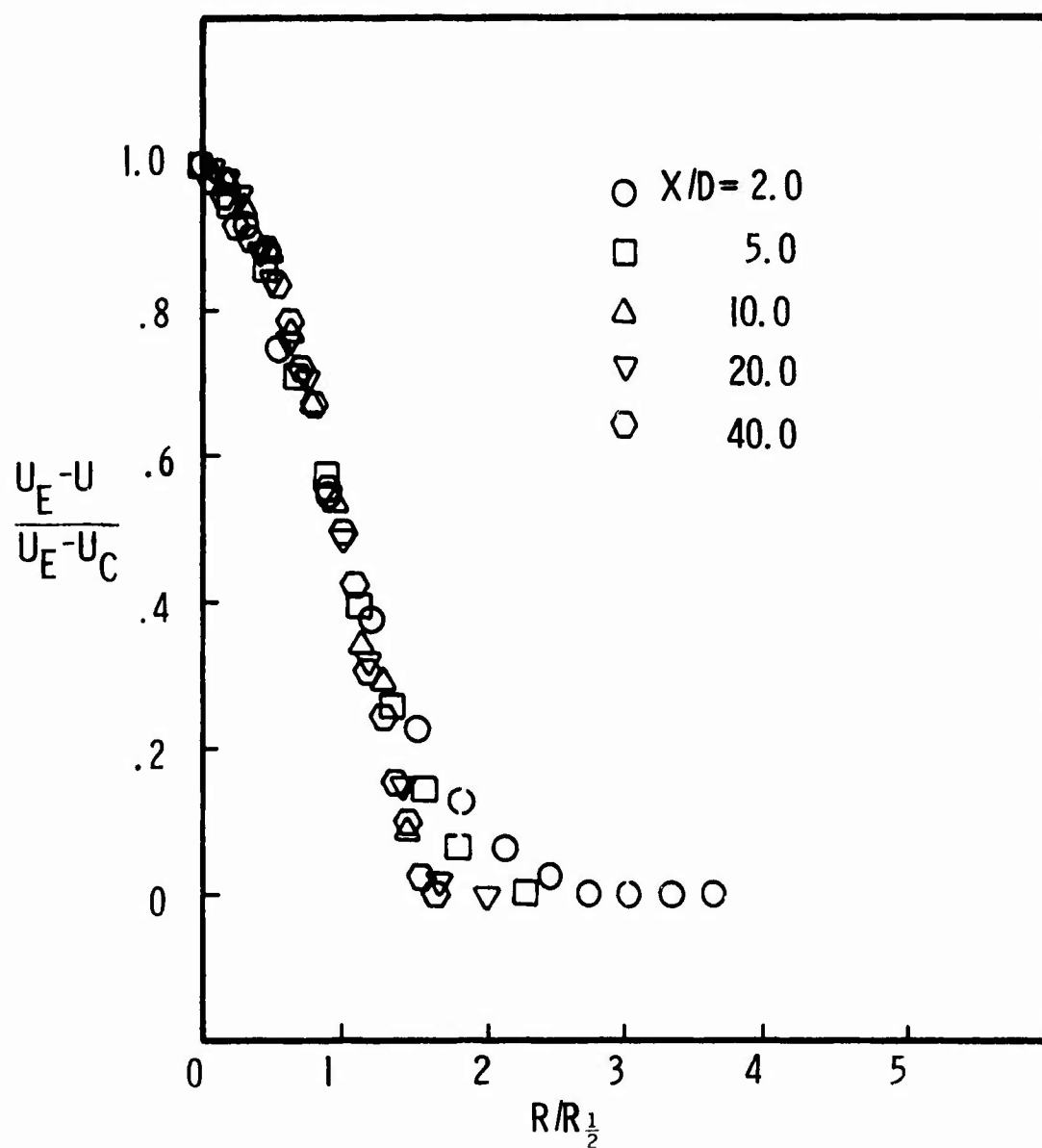
FIG. 12   SELF-SIMILARITY VELOCITY PROFILES —
MODEL# 1 ($V_\infty = 101$ ft/sec)
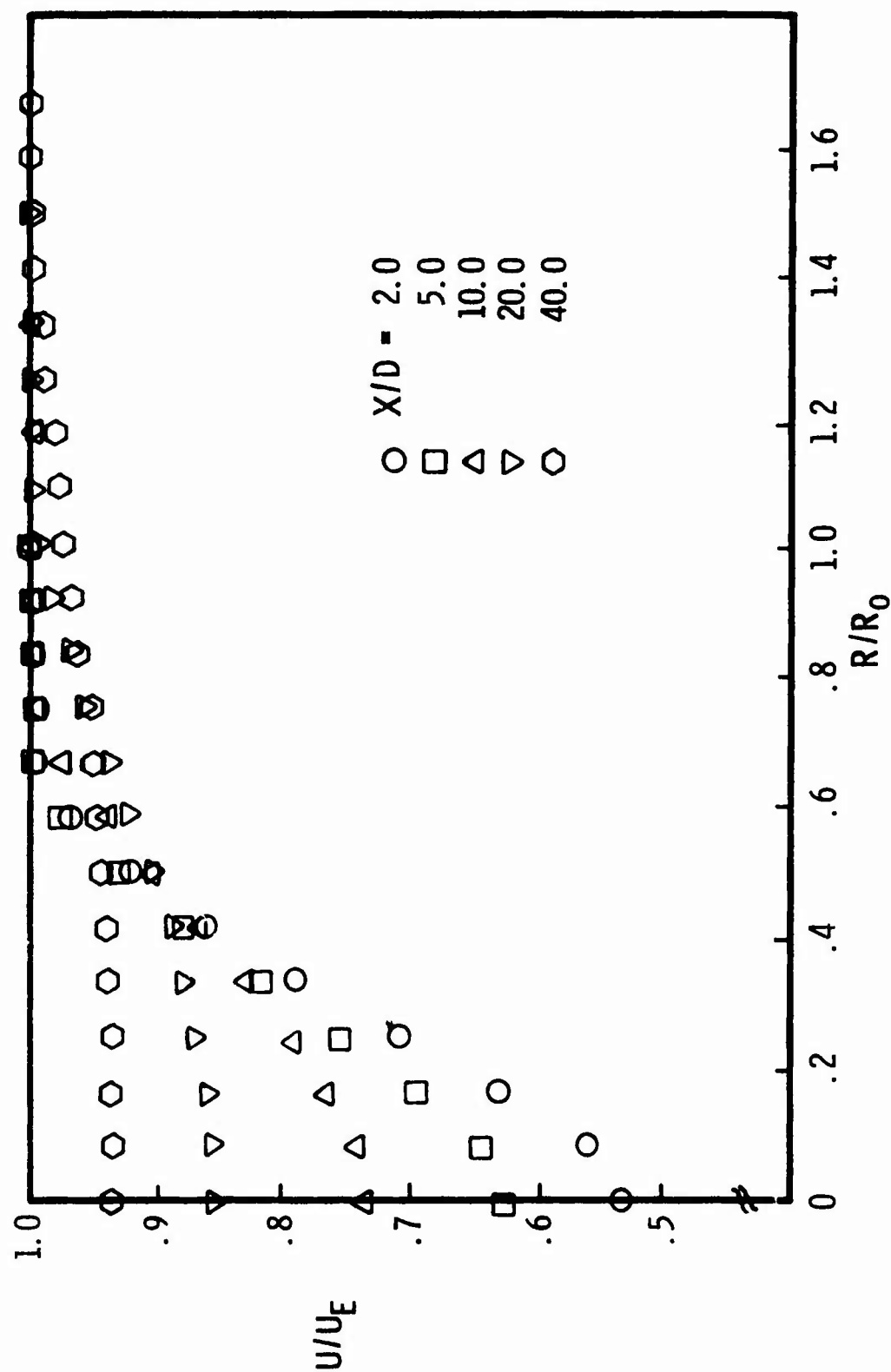
FIG. 13 MEAN AXIAL VELOCITY PROFILES -- MODEL#1 (V_∞ = 206 ft/sec)
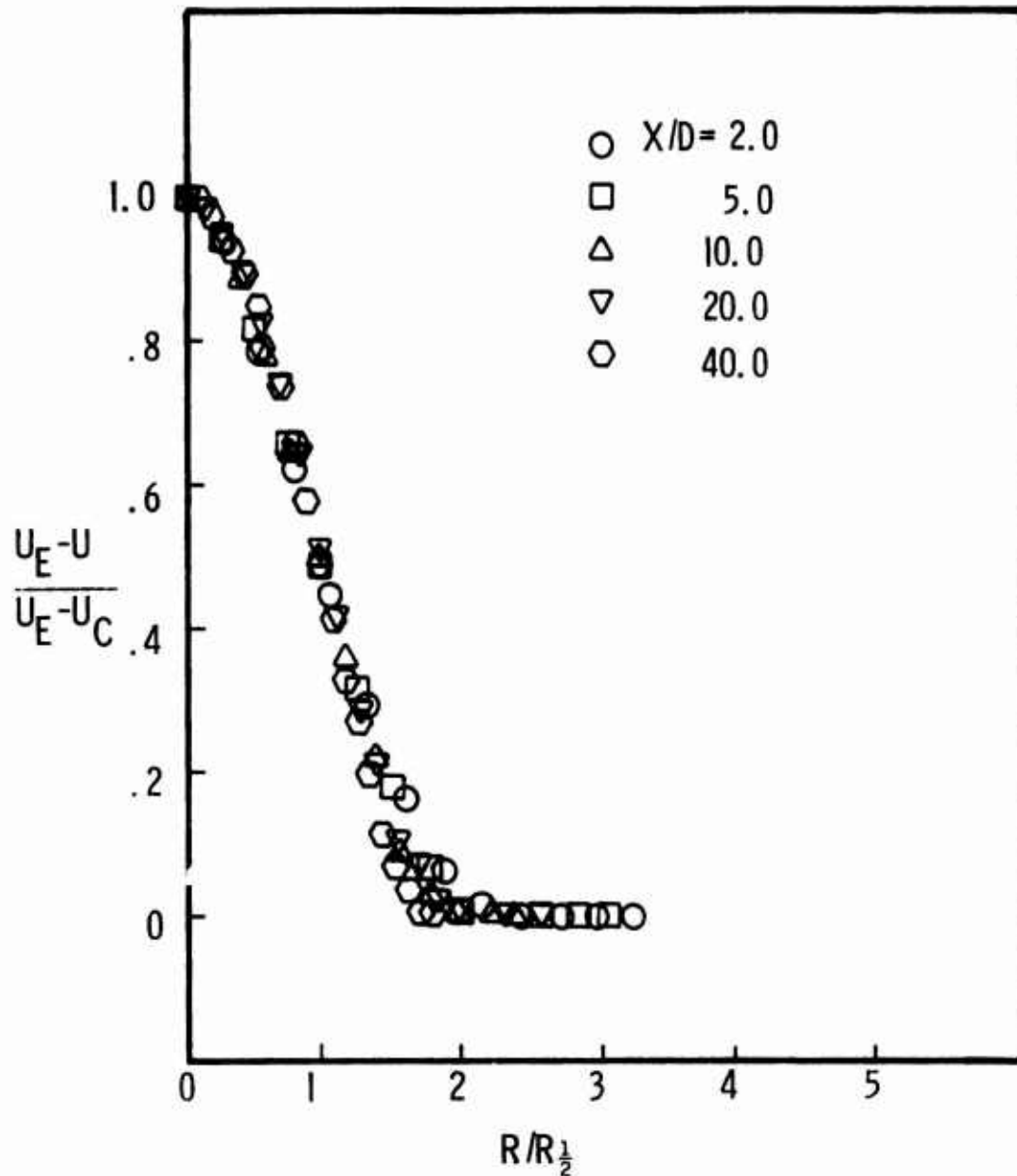
FIG. 14   SELF-SIMILARITY VELOCITY PROFILES —
MODEL# 1 ($V_\infty = 206$ ft/sec)
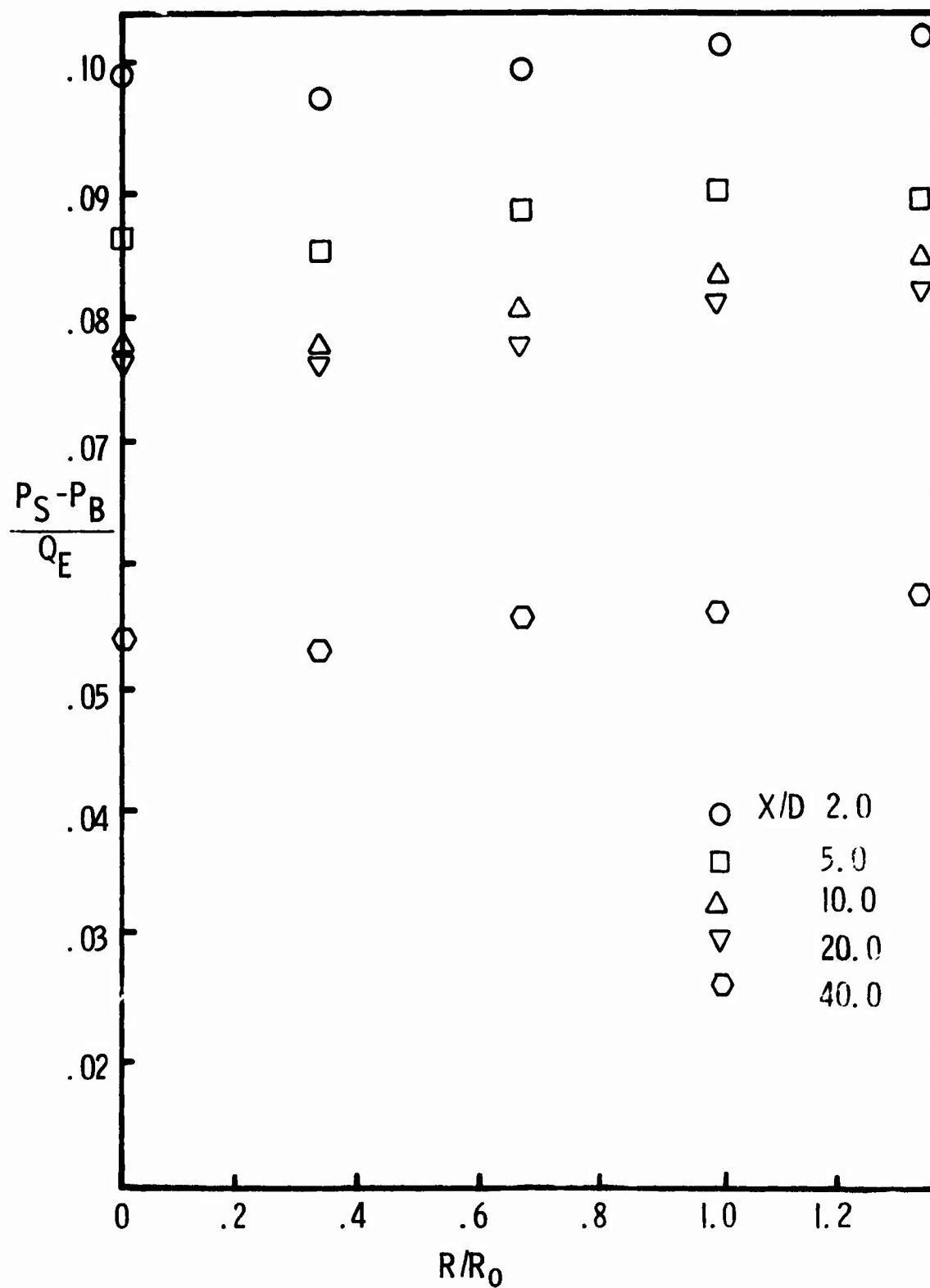
FIG. 15   STATIC PRESSURE PROFILES —— MODEL#1
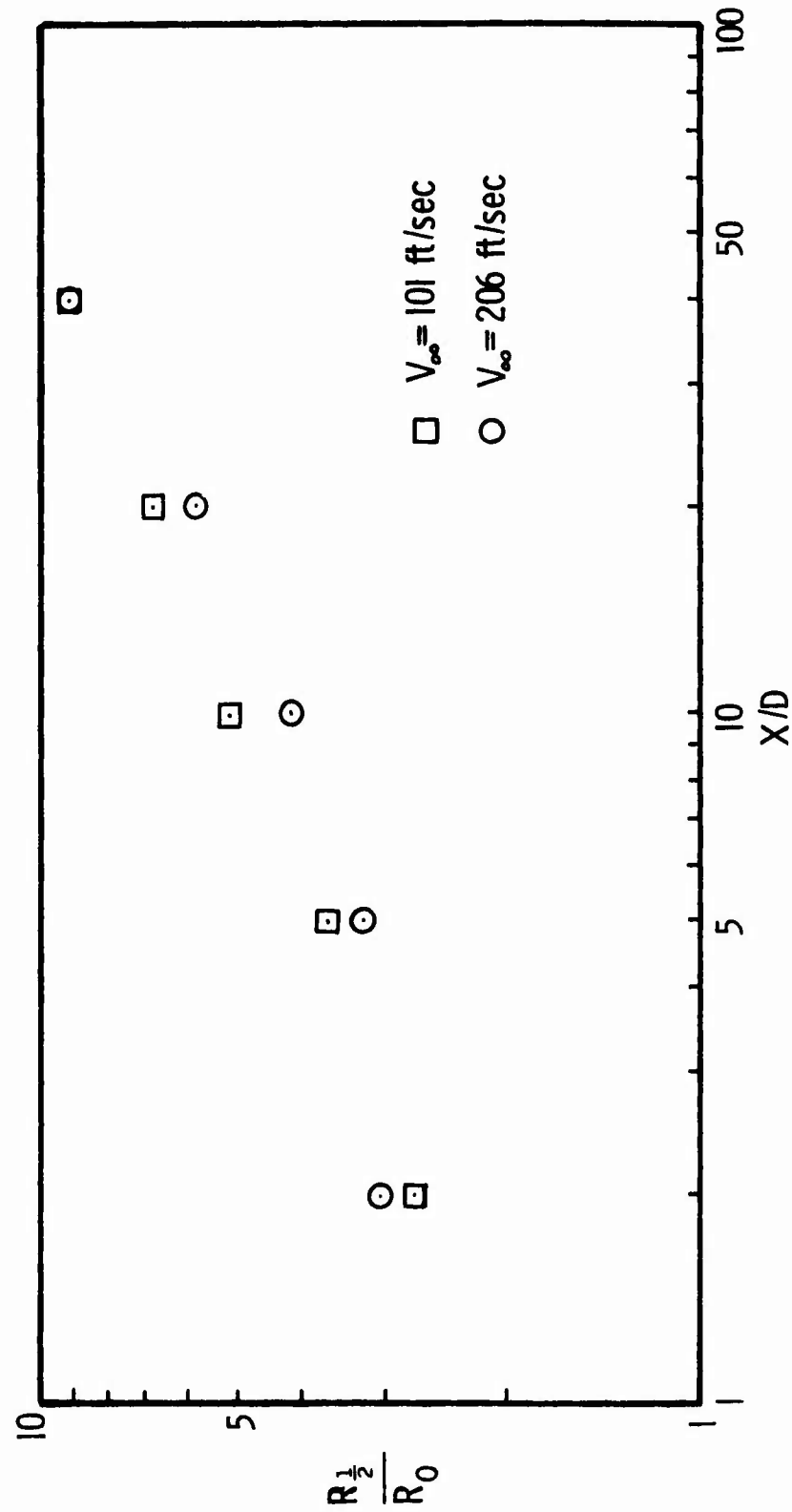
FIG 16   AXIAL GROWTH OF WAKE — MODEL #1
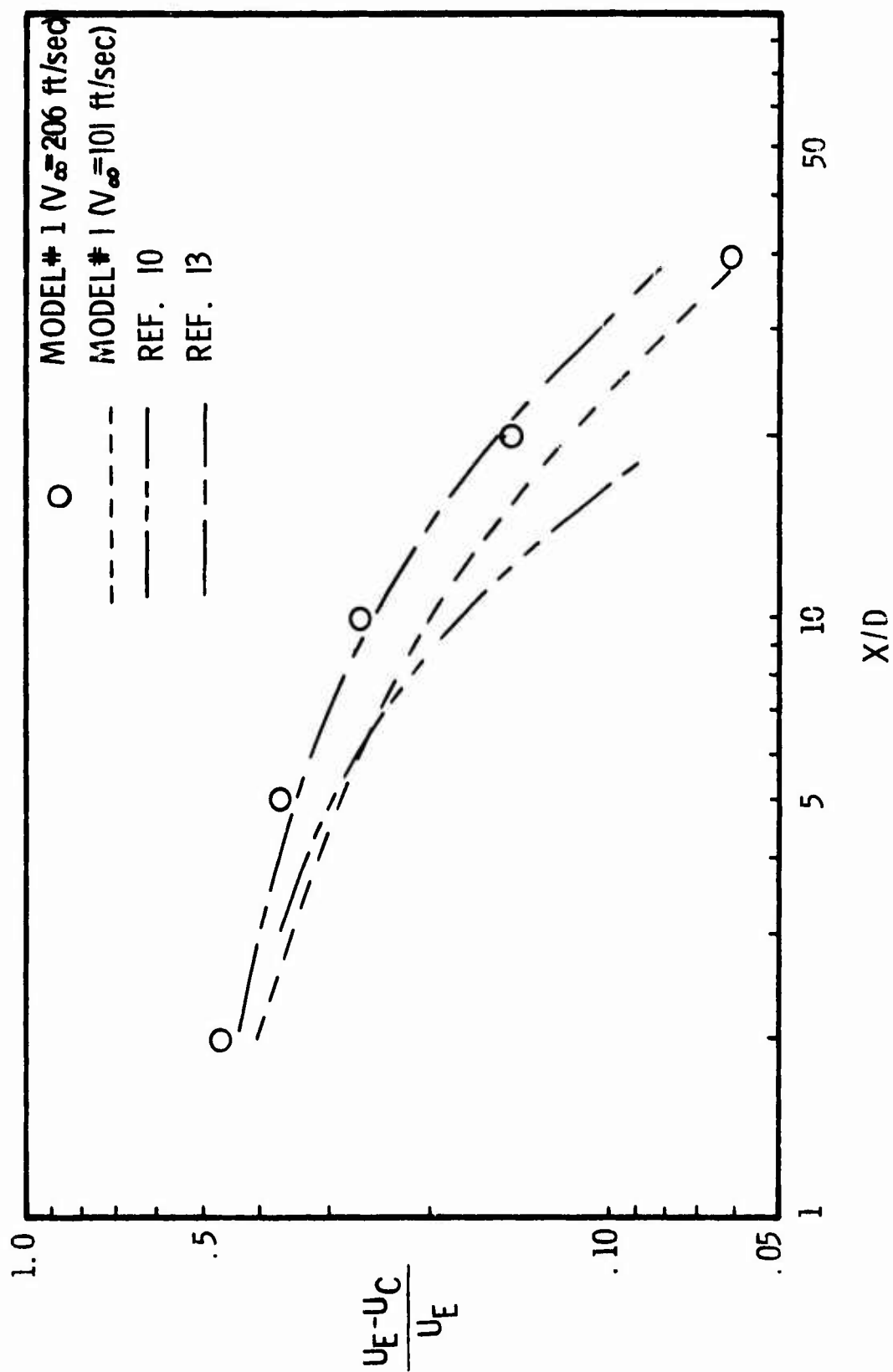
FIG. 17 COMPARISONS OF AXIAL VELOCITY DEFICIT DECAY
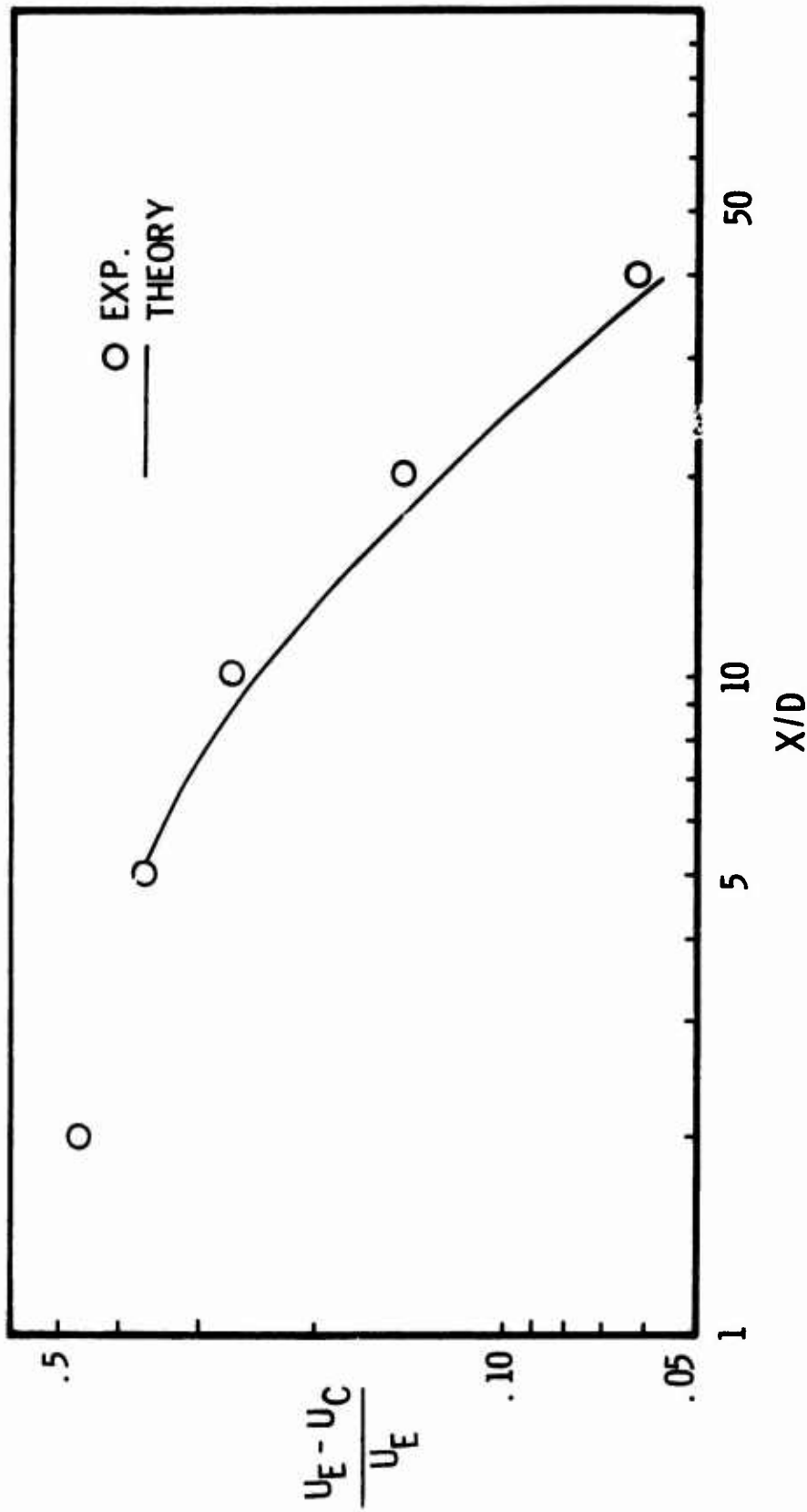
FIG. 18 AXIAL VELOCITY DEFICIT VS. X/D -- MODEL# 1
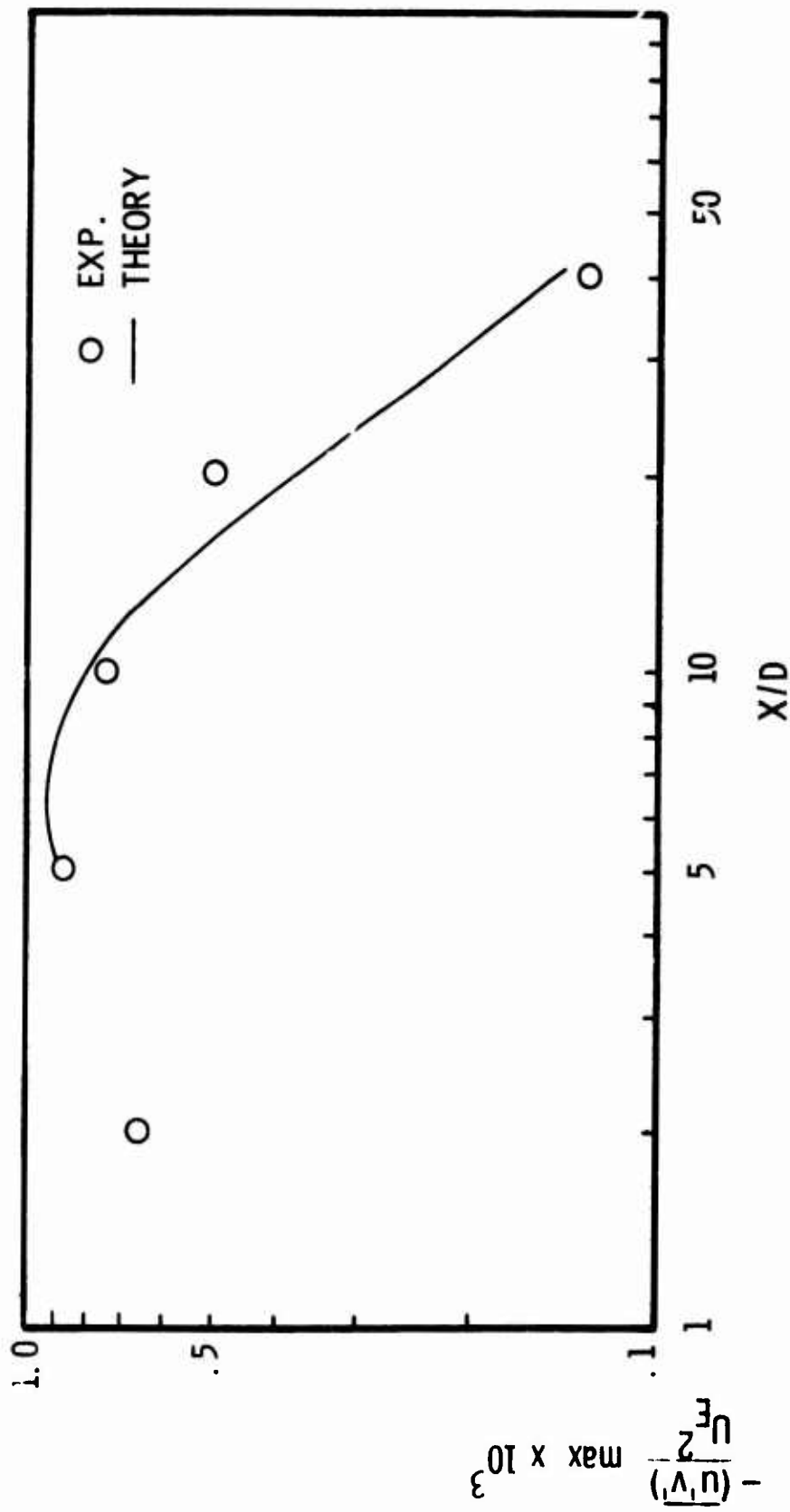
FIG. 19 X/D DECAY OF MAXIMUM SHEAR STRESS -- Model #1
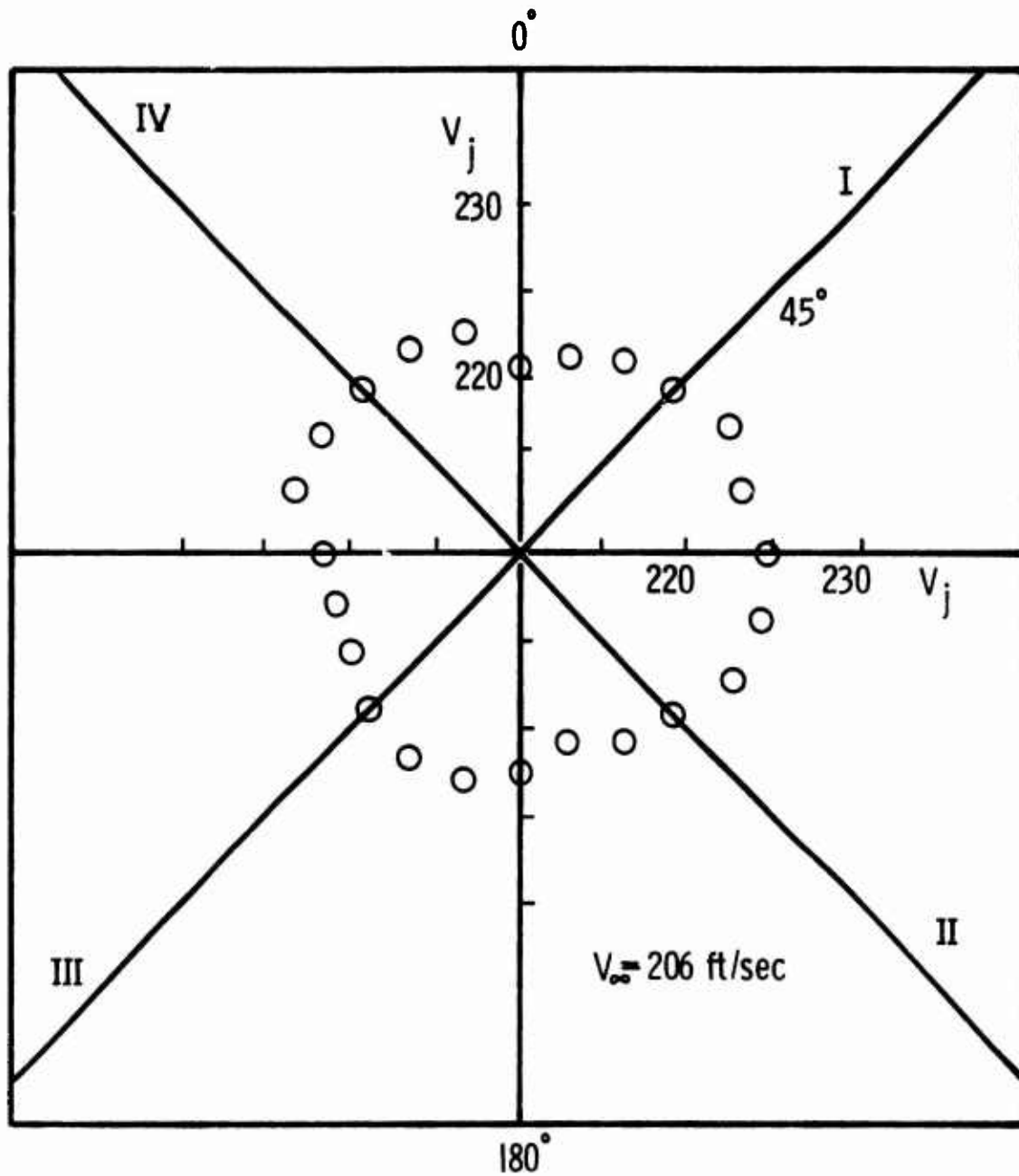
FIG. 20   POLAR GRAPH OF JET VELOCITY VS.
PERIPHERAL ANGLE
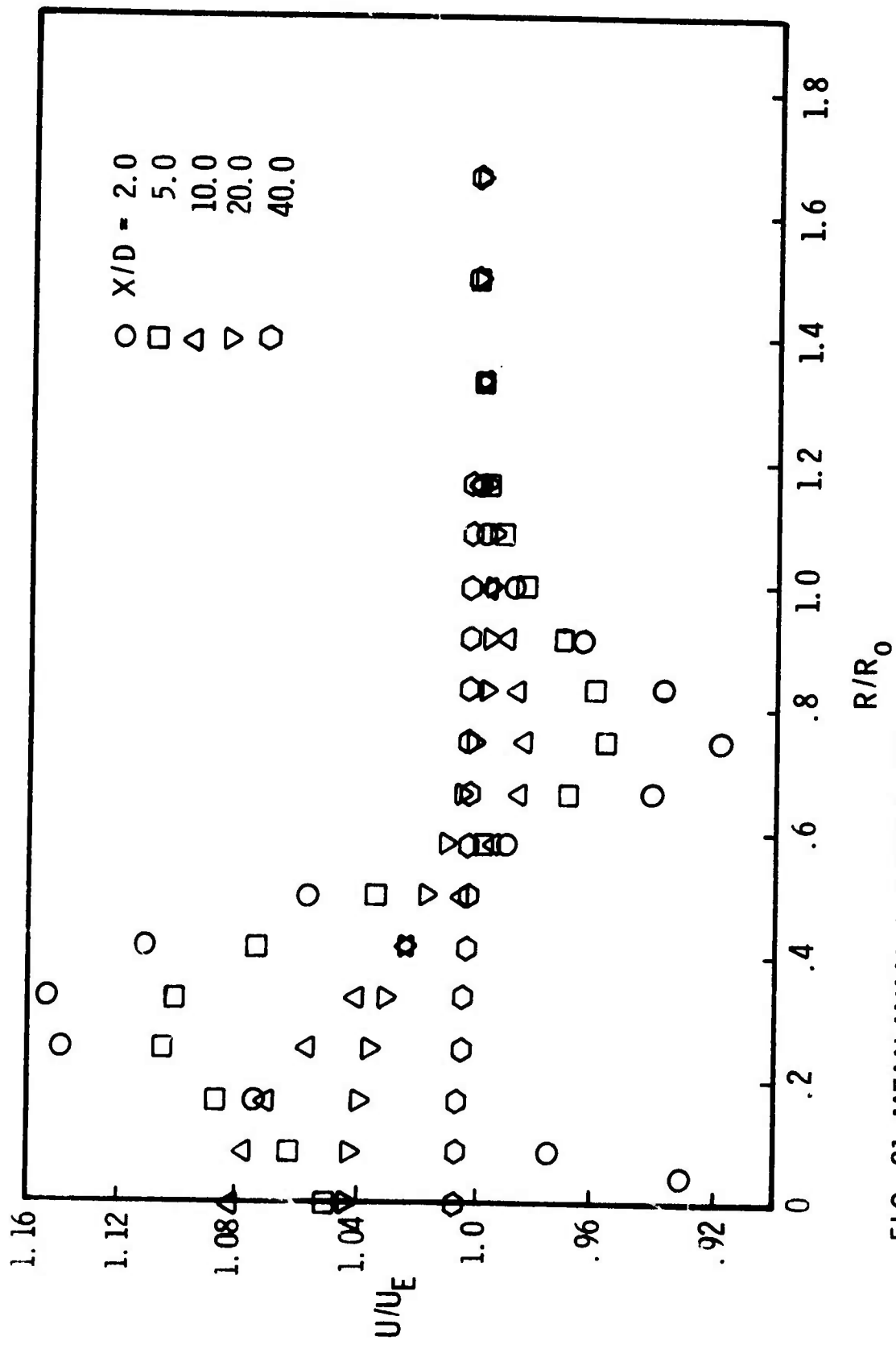
FIG. 21 MEAN AXIAL VELOCITY PROFILES -- MODEL# 2
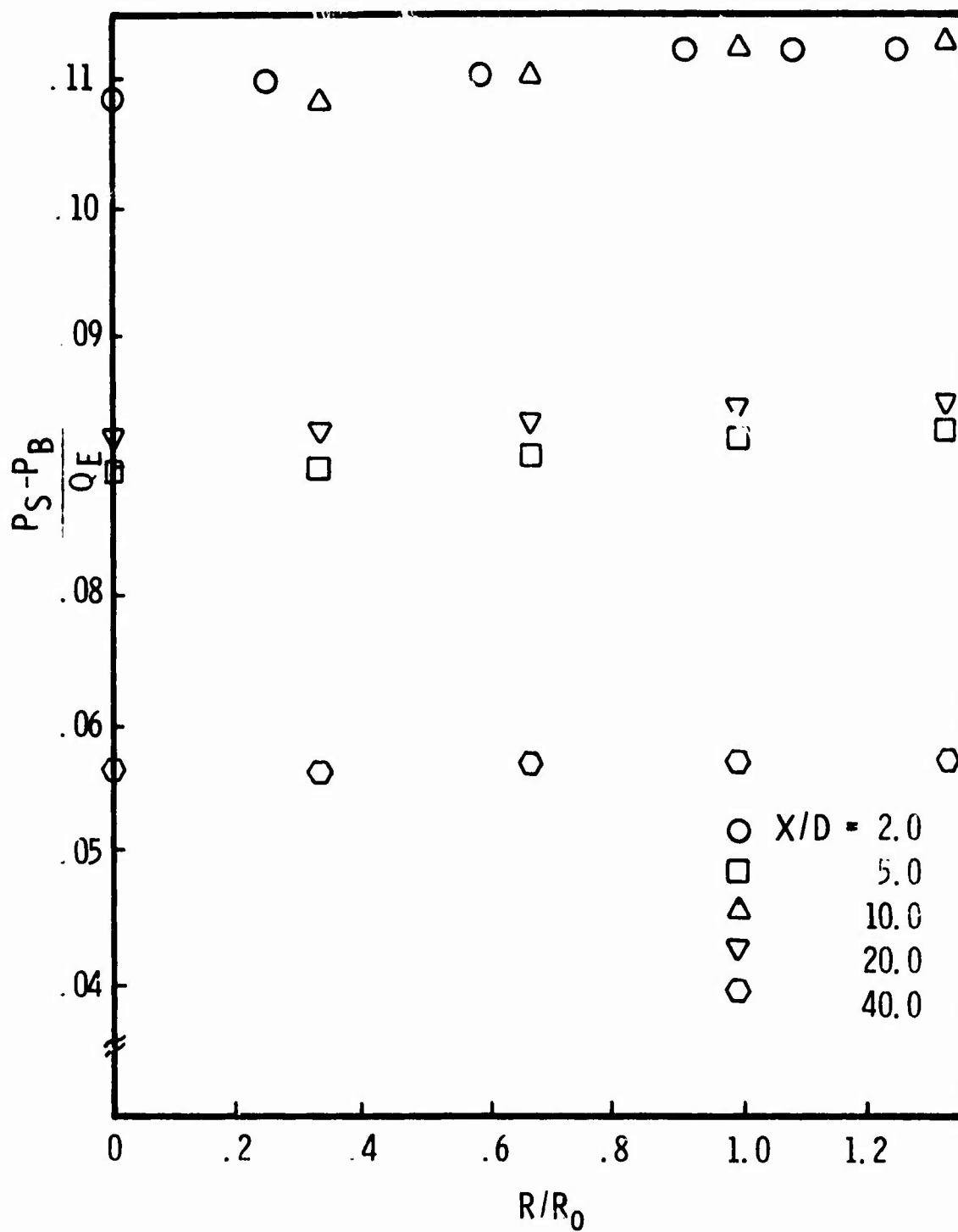
FIG. 22 STATIC PRESSURE PROFILES -- MODEL# 2
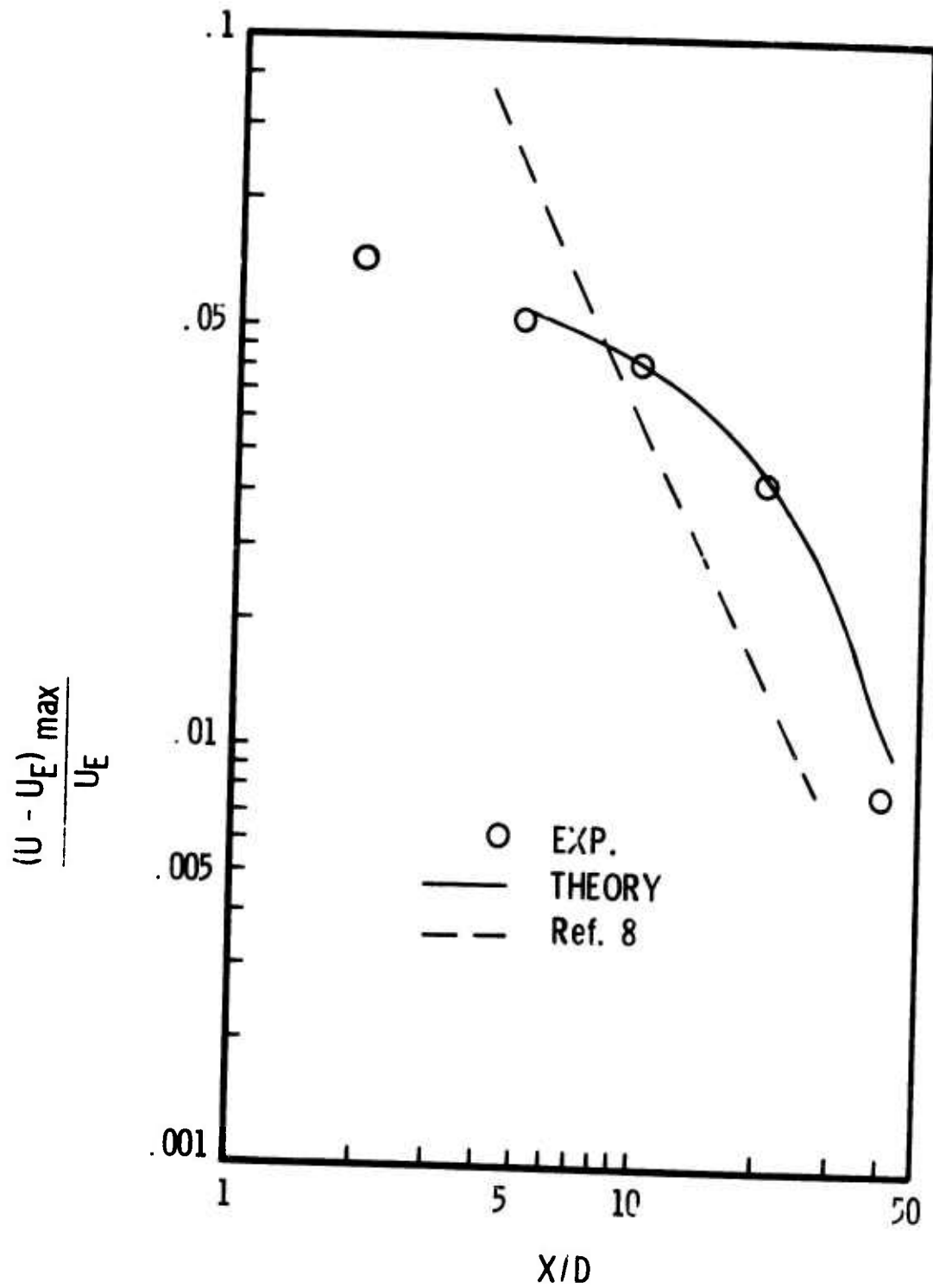
FIG. 23   MAXIMUM VELOCITY EXCESS VS. X/D
MODEL #2
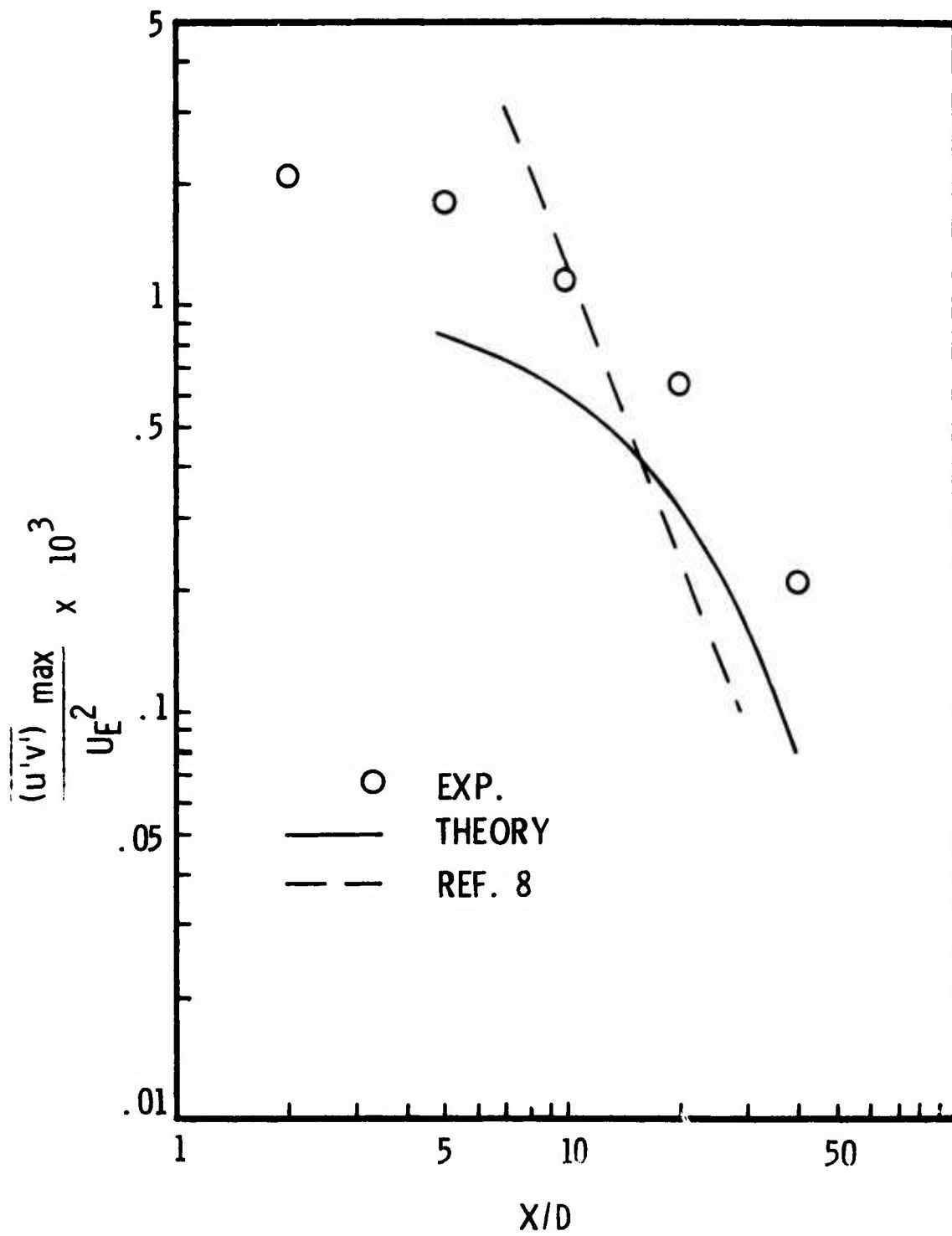
FIG. 24 X/D DECAY OF MAXIMUM SHEAR STRESS --
        MODEL#2
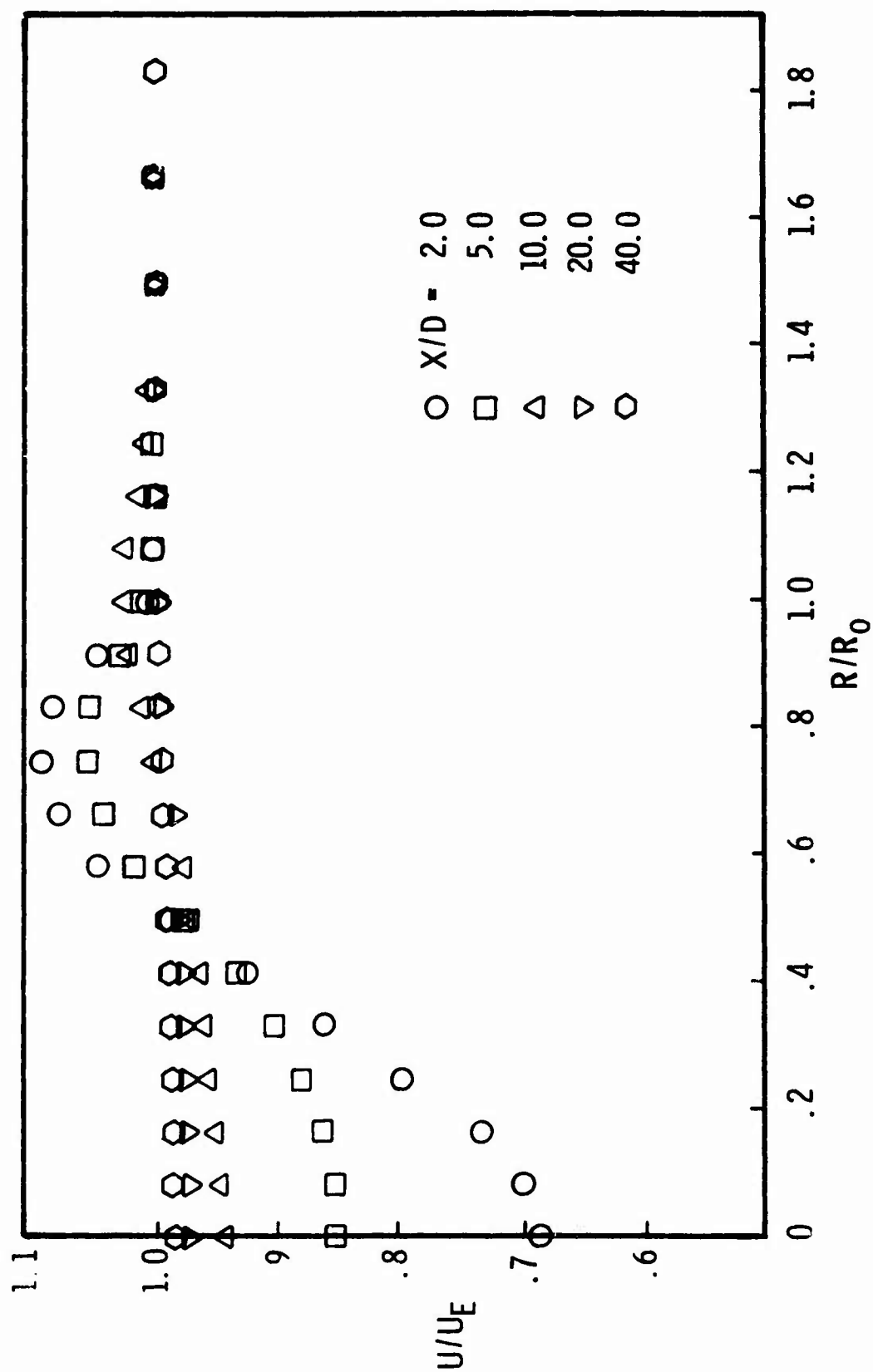
FIG. 25 MEAN AXIAL VELOCITY PROFILES -- MODEL#3
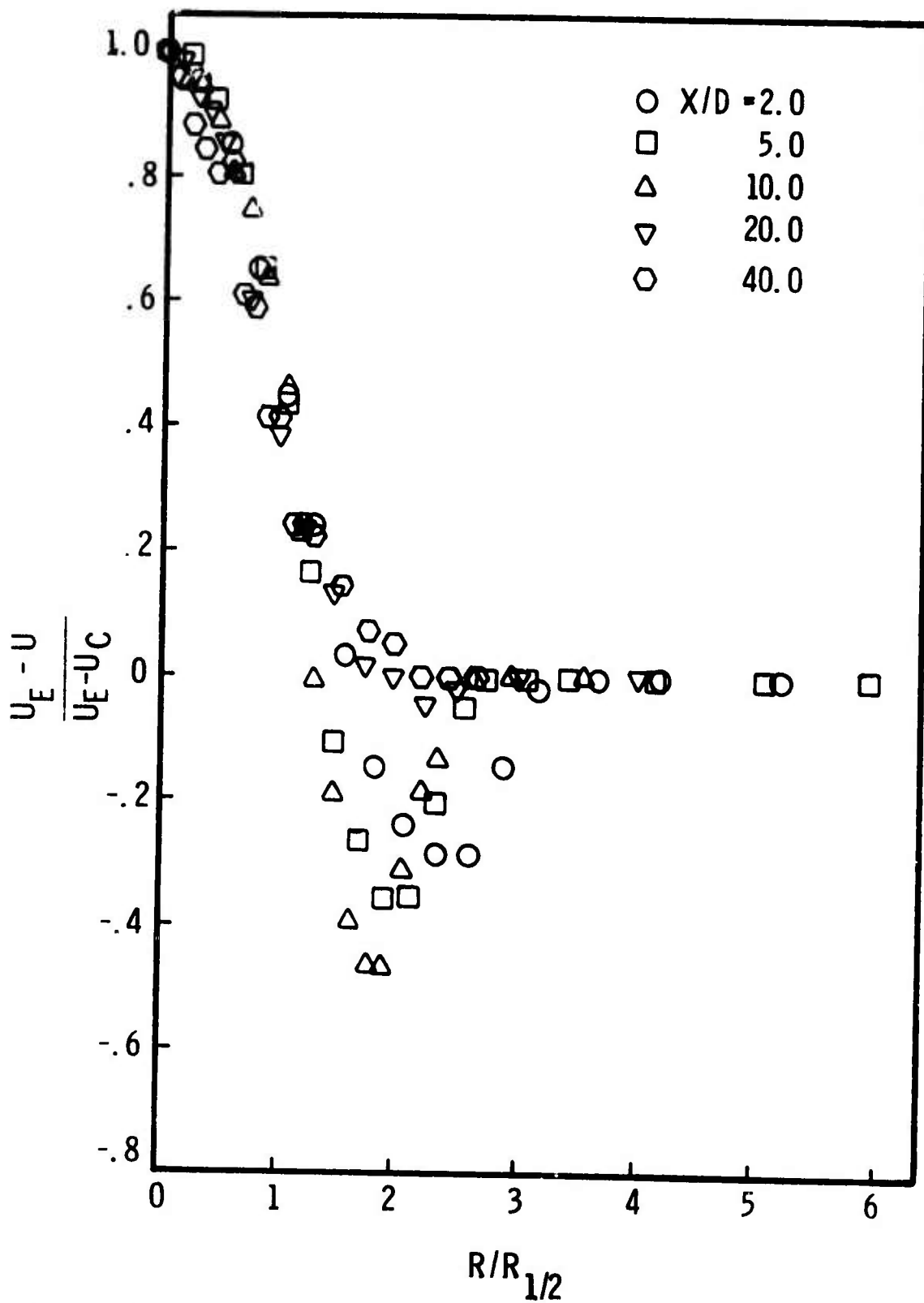
Fig. 26 VELOCITY PROFILES IN SELF-SIMILAR FORM --
MODEL # 3
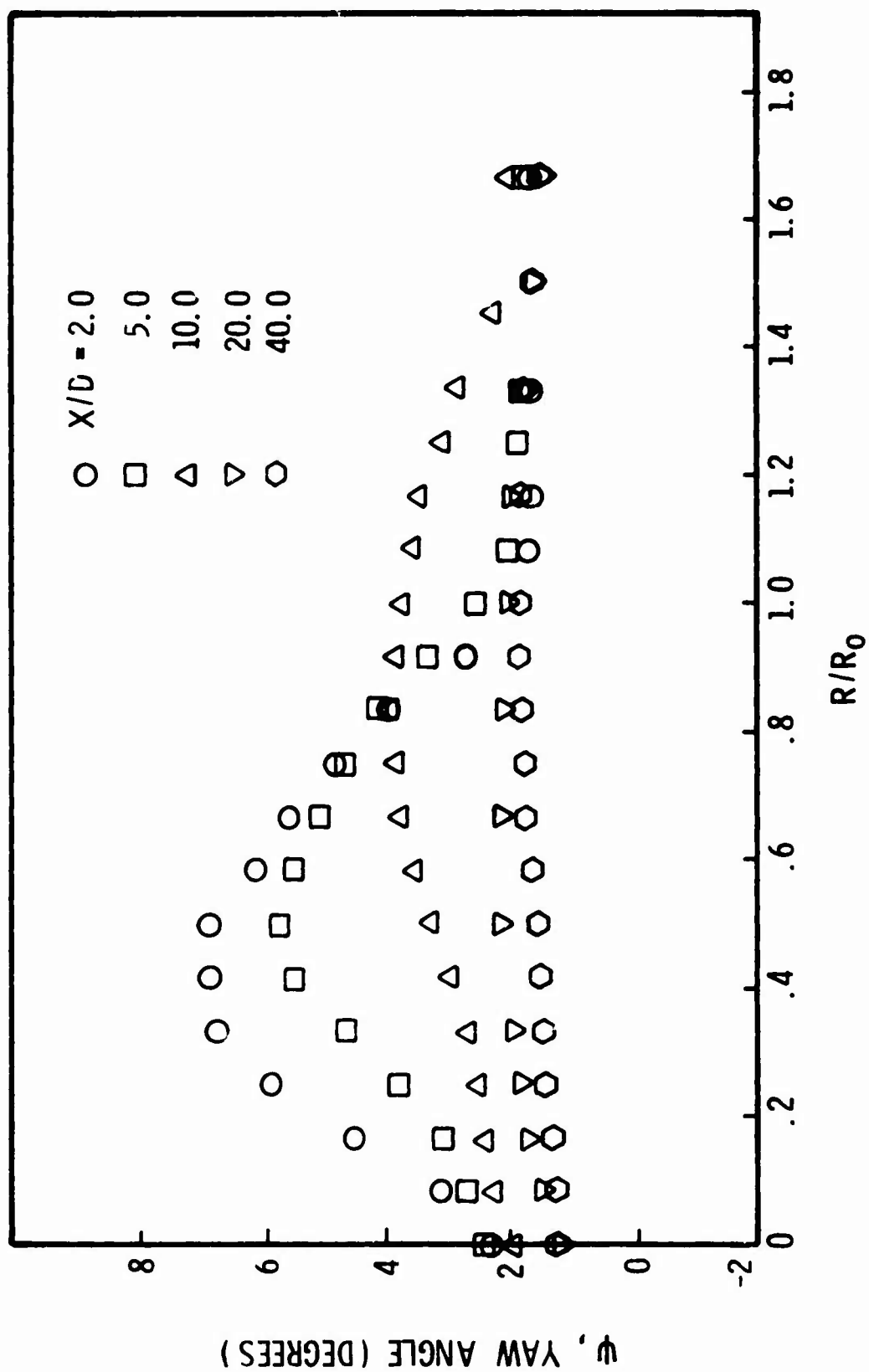
FIG. 27 YAW ANGLE DISTRIBUTIONS
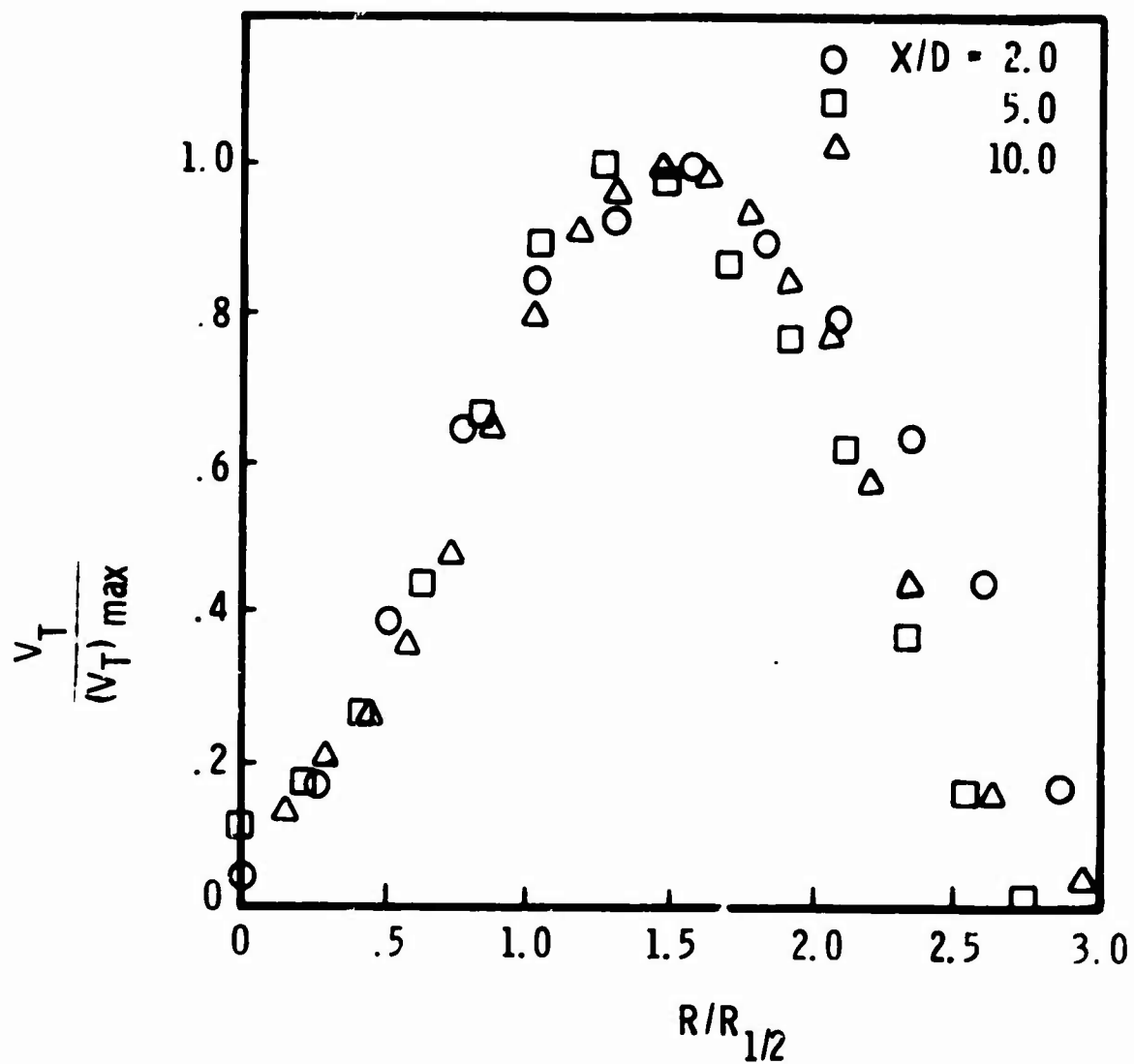
Fig. 28 TANGENTIAL VELOCITY PROFILES IN
SELF-SIMILAR FORM -- MODEL #3
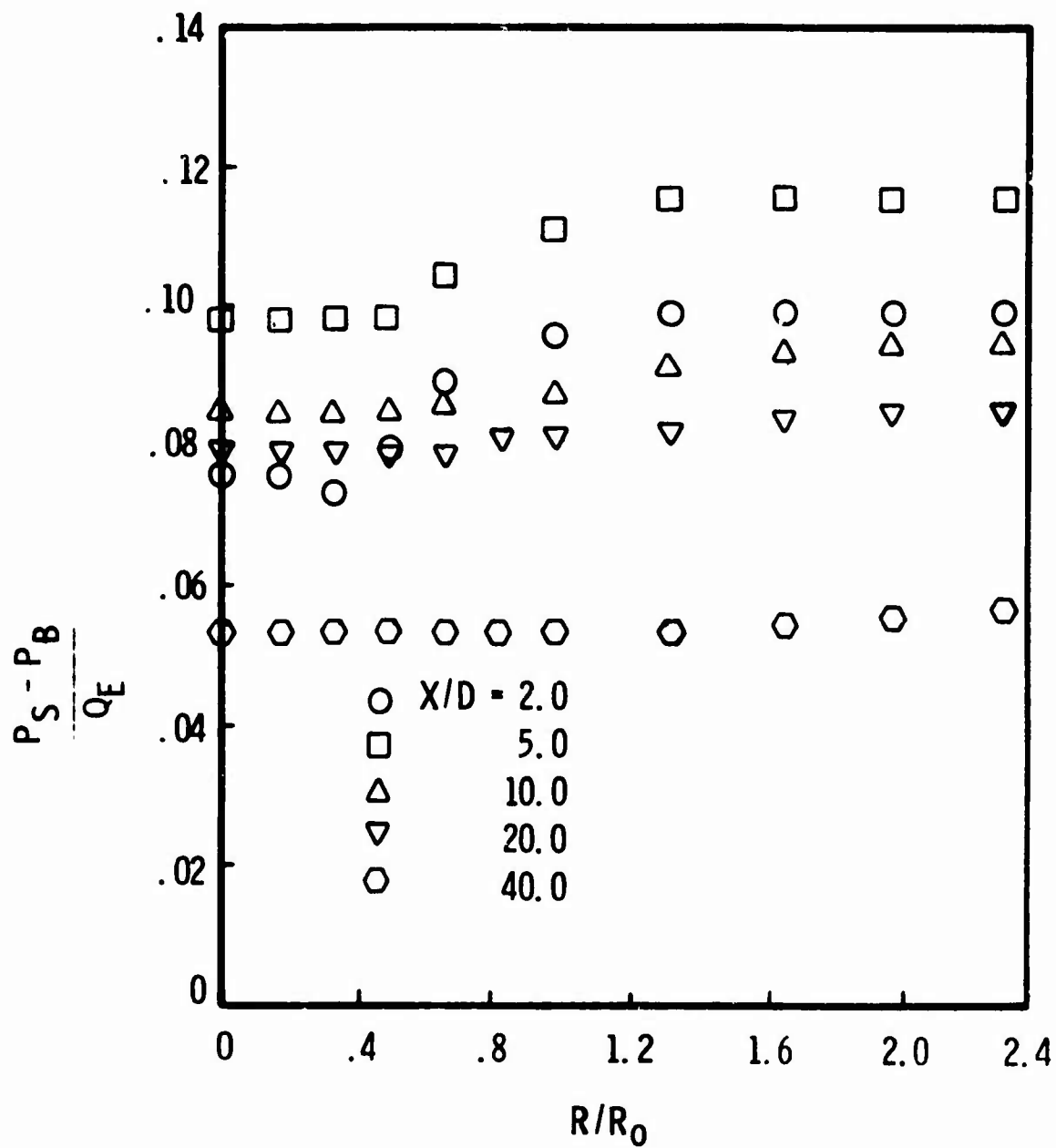
FIG. 29   STATIC PRESSURE PROFILES -- MODEL #3
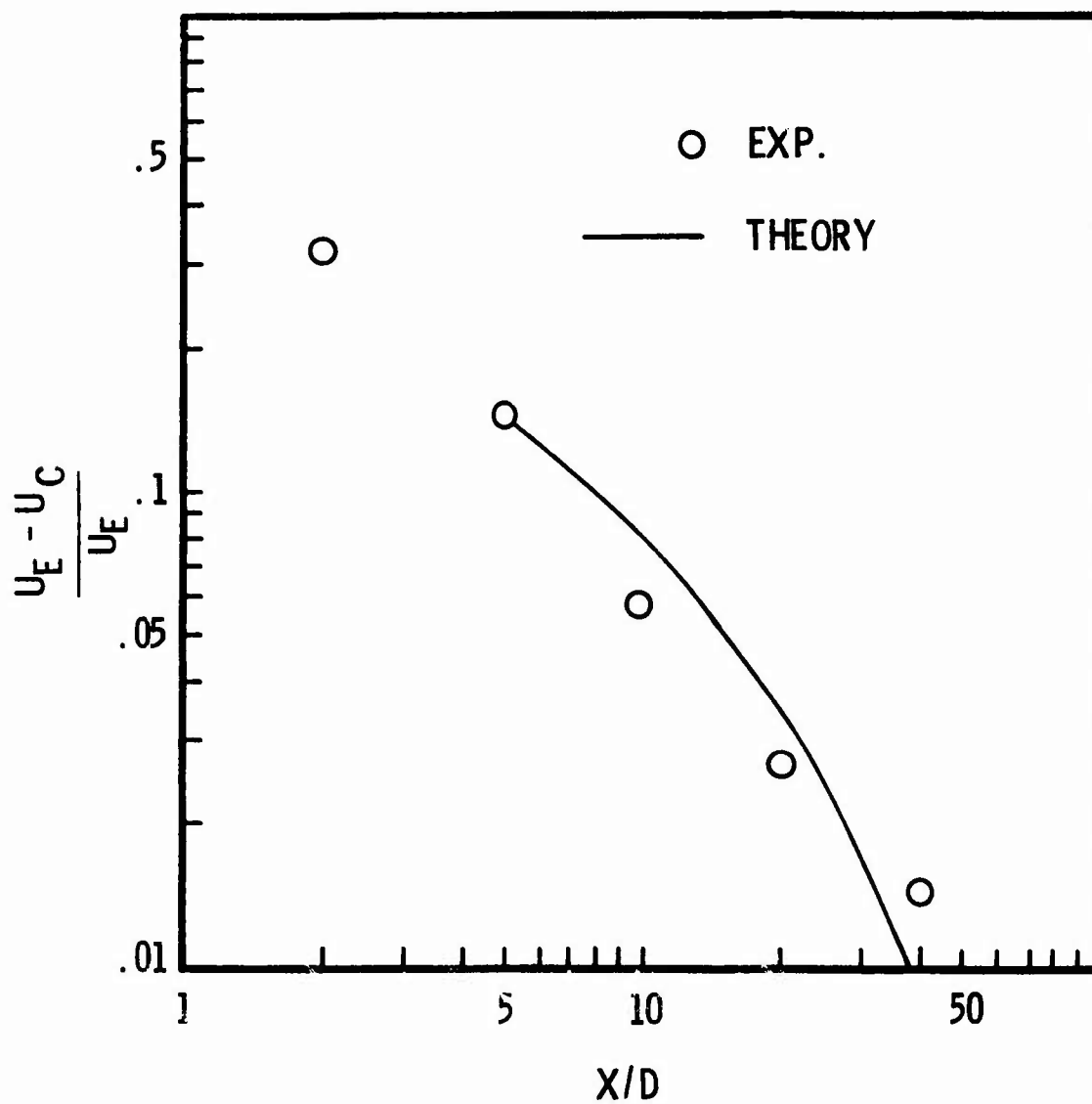
FIG. 30   VELOCITY DEFICIT VS. X/D -- MODEL# 3
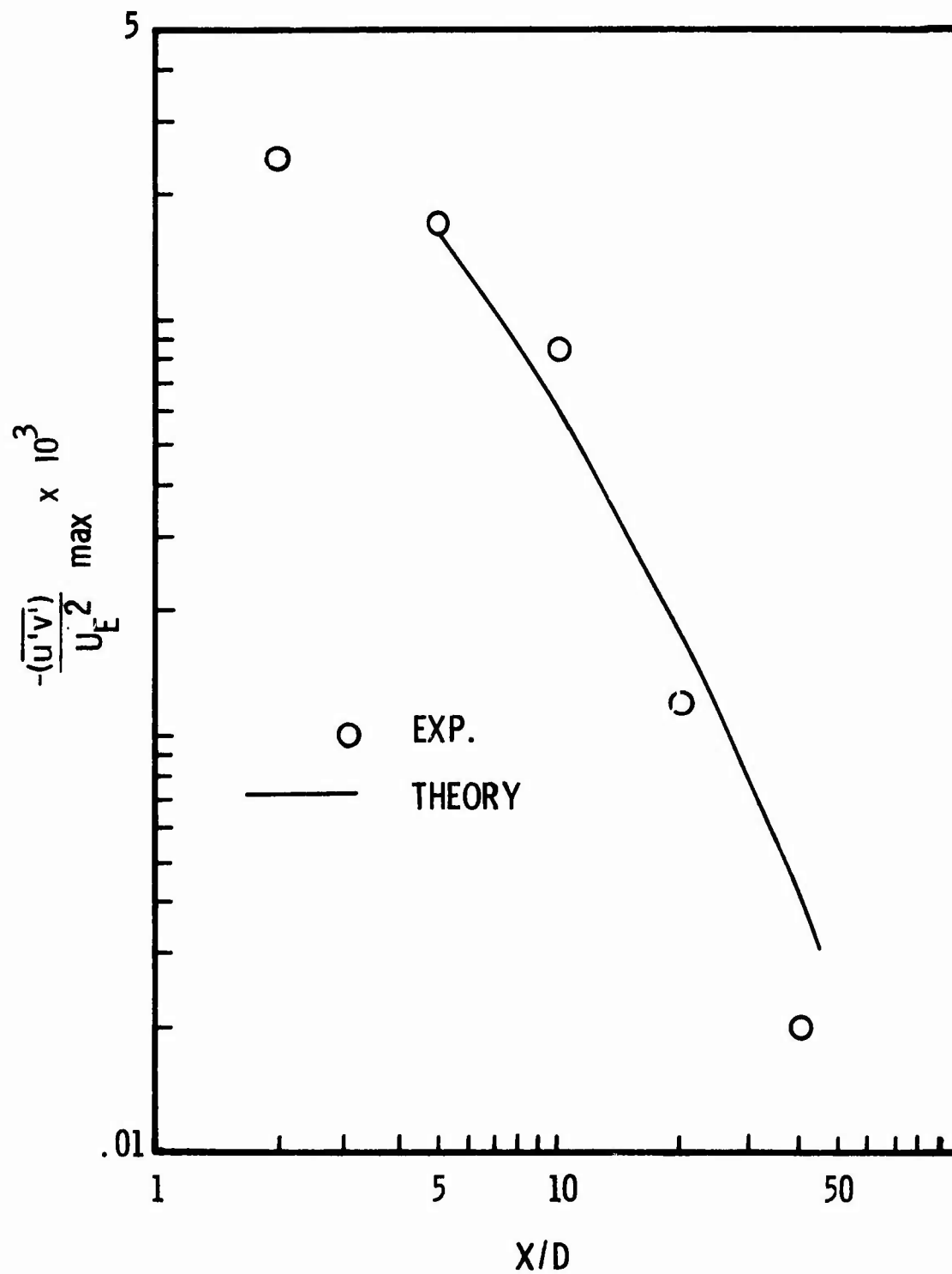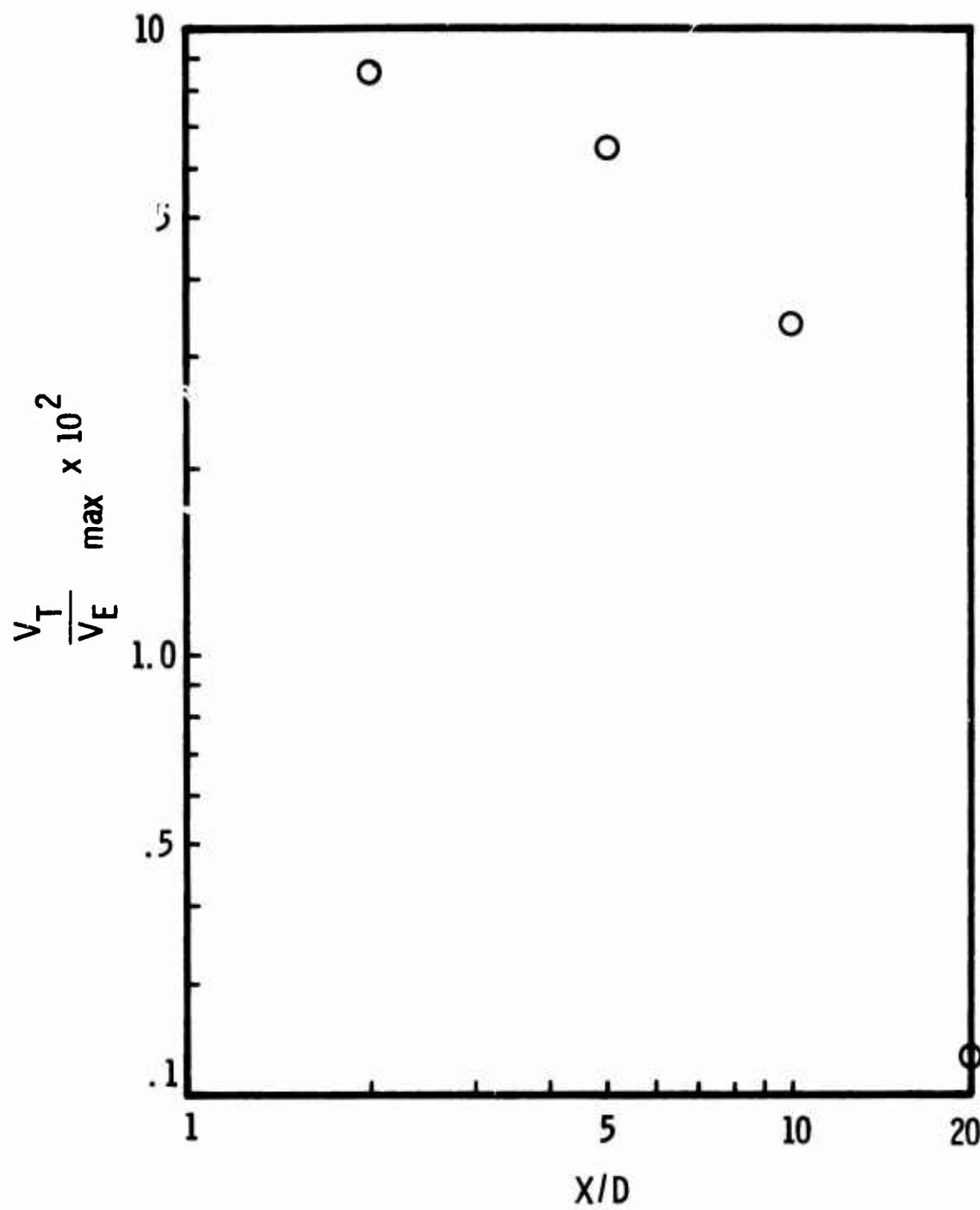
FIG. 31 X/D DECAY OF MAXIMUM SHEAR STRESS --
MODEL# 3

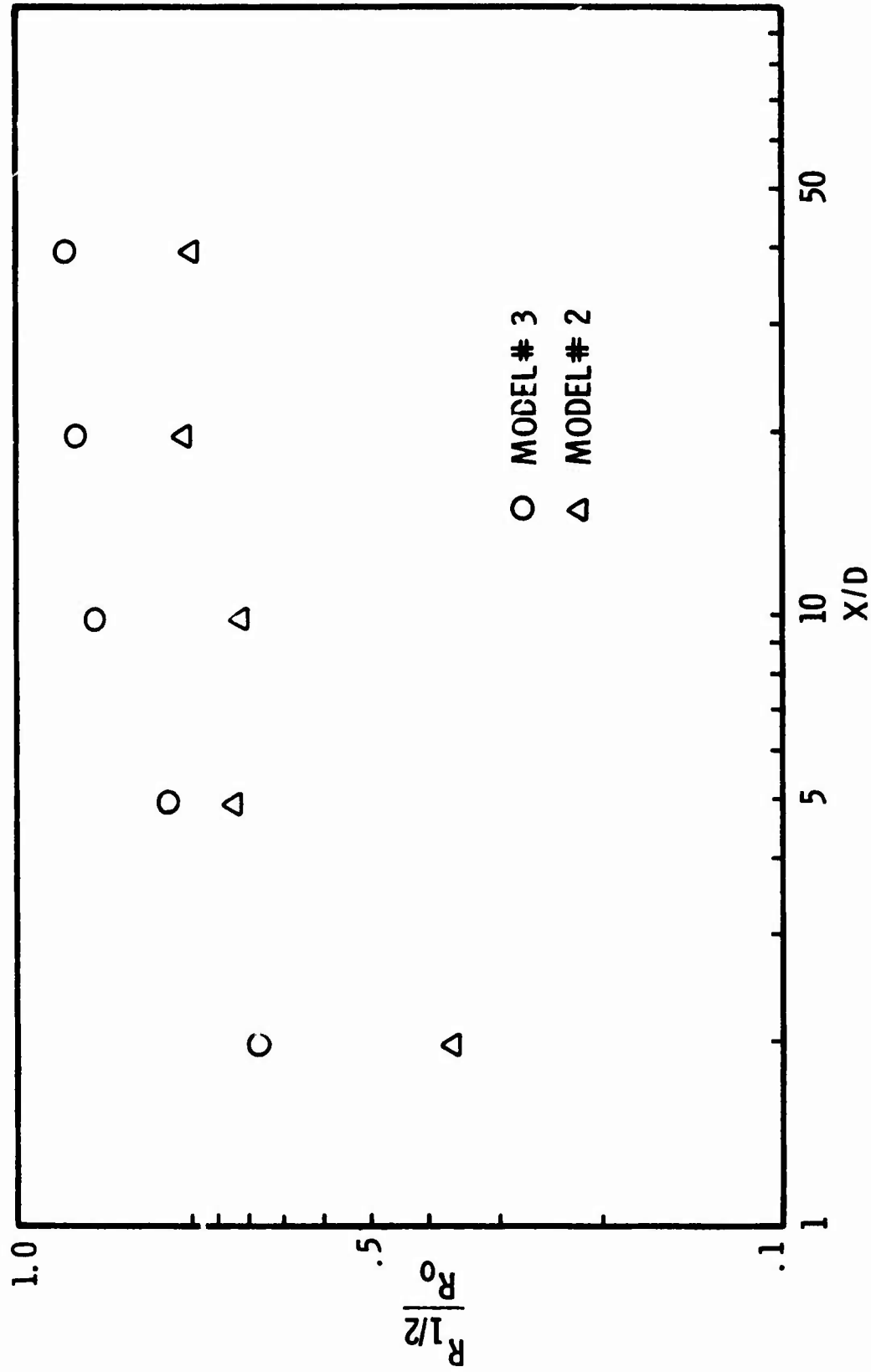FIG. 32   AXIAL DECAY OF TANGENTIAL VELOCITY
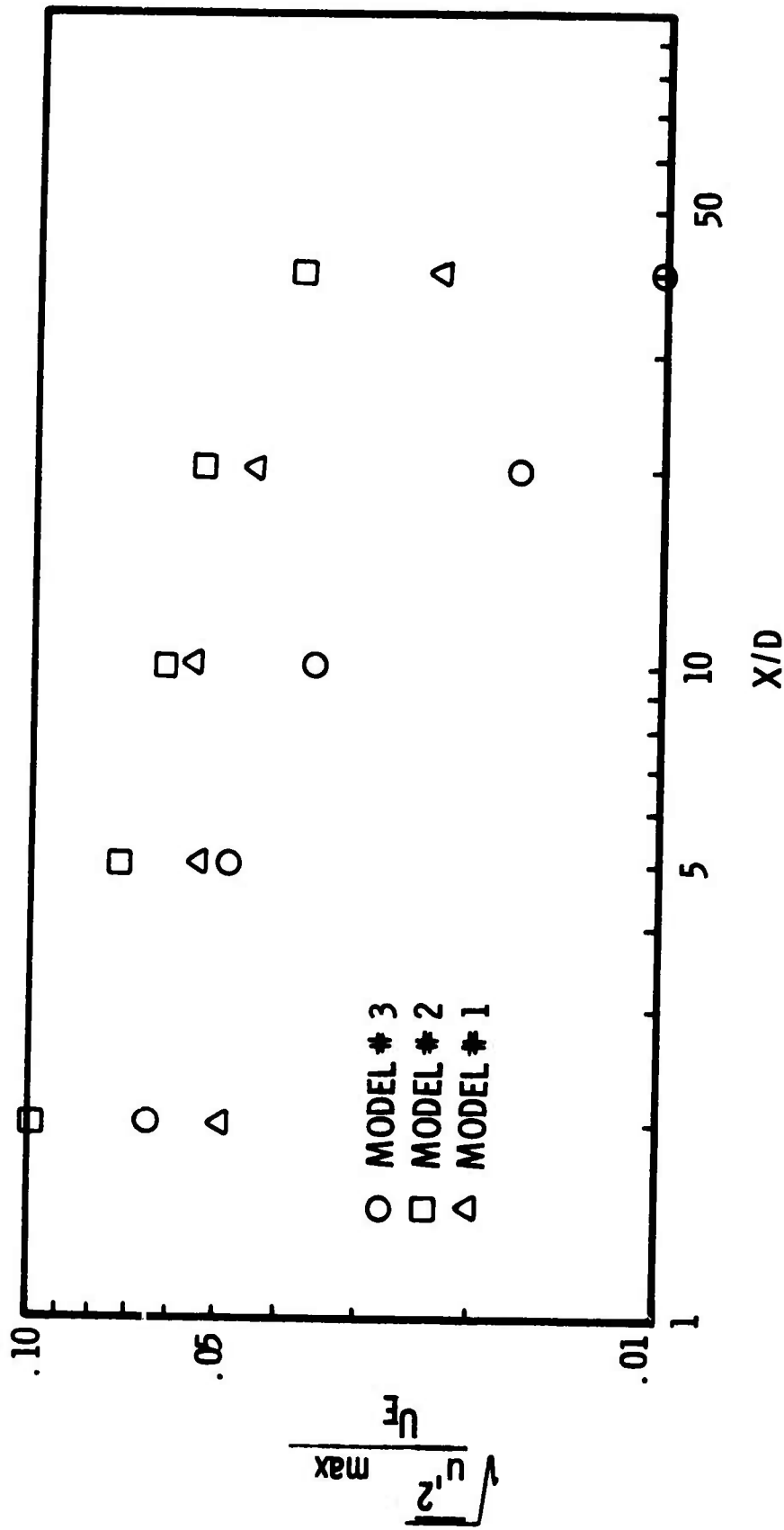
FIG. 33   AXIAL GROWTH OF WAKE -- MODELS # 2 and # 3

FIG. 34   X/D DECAY OF MAXIMUM AXIAL TURBULENCE INTENSITY